Geological Magazine

www.cambridge.org/geo

Original Article

Cite this article: Dey A, Sen K, and Mamtani MA (2023) Lattice preferred orientation of quartz in granitic gneisses from Tso Morari Crystalline Complex, Eastern Ladakh, trans-Himalaya: evaluating effect of Dauphiné twin in dynamic recrystallization during exhumation. *Geological Magazine* **160**: 1556–1577. https://doi.org/10.1017/S0016756823000560

Received: 31 May 2022
Revised: 27 July 2023
Accepted: 1 September 2023
First published online: 4 October 2023

Keywords:
Dauphiné twin; Electron backscatter diffraction; Lattice preferred orientation; Misorientation analysis; Quartz

Corresponding author:
Koushik Sen; Email: koushik.geol@gmail.com

Lattice preferred orientation of quartz in granitic gneisses from Tso Morari Crystalline Complex, Eastern Ladakh, trans-Himalaya: evaluating effect of Dauphiné twin in dynamic recrystallization during exhumation

Alosree Dey[1,2], Koushik Sen[1,2] and Manish A. Mamtani[3]

[1]Wadia Institute of Himalayan Geology, 33 GMS Road, Dehradun 248001, India; [2]Academy of Scientific and Innovative Research, Ghaziabad 201002, Uttar Pradesh, India and [3]Department of Geology and Geophysics, Indian Institute of Technology, Kharagpur 721302, India

Abstract

The Tso Morari Crystalline complex (TMCC) of eastern Ladakh, India, is part of the north Indian continental margin and is characterized by eclogitic enclaves embedded within ortho- and paragneisses known as the Puga Gneiss. Two fault zones bound the TMCC: the Karzok fault to the southwest and the Zildat fault to the northeast. In the present study, we carried out Electron Backscatter Diffraction study of quartz of 10 samples collected from the Puga Gneiss. The relict and recrystallized quartz grains were treated separately to understand the deformation conditions of the Puga Gneiss during early and late deformation stages related to UHP metamorphism and final stage of exhumation during retrogression, respectively. Microstructural observations suggest dynamic recrystallization in quartz and plagioclase at different temperature ranges. Misorientation analysis of both relict and recrystallized quartz grains reveals presence of Dauphiné Twins. Lattice preferred Orientation (LPO) of <c> axis of relict quartz grains generally shows more than one point maxima indicating that the relict grains preserve LPO developed during different stages of metamorphism/deformation. On the other hand, LPO of <c> axis of recrystallized grains from Karzok and Zildat fault zones shows asymmetric single girdle either normal or at an angle to the foliation plane, which suggests simple shear. We conclude that grain size reduction and recrystallization of the Puga Gneiss was greatly influenced by Dauphiné Twin and the final exhumation of the TMCC took place in a simple shear environment aided by activity along its two binding fault zones.

1. Introduction

Quartz is the most abundant rock-forming mineral of the continental crust, and its dynamic recrystallization processes greatly influence the rheological properties of crustal rocks. Lattice preferred orientation (LPO) of quartz has long been investigated to understand the regime and magnitude of strain along with mechanisms and temperature of deformation (e.g. Schmid & Casey, 1986; Law, 1990, 2014; Neumann, 2000; Trepmann & Stökhert, 2003; Heilbronner & Tullis, 2006; Trepmann et al. 2007; Thigpen et al. 2010; Faleiros et al. 2016, Cross et al. 2017; Kilian & Heilbronner, 2017). Electron backscatter diffraction (EBSD) is one of the most widely used methods for LPO analysis of common rock-forming minerals (Mainprice & Nicolas, 1989; Prior et al. 1999, 2009). Quartz LPO is developed due to dislocation creep mechanism. However, dynamic recrystallization and the development of LPO in quartz are intricately related as dynamic recrystallization can either destroy the pre-existing LPO or modify or mimic it or develop new LPO (Otani & Wallis, 2006; Vernooij et al. 2006; Wightman et al. 2006; Trepmann et al. 2017 and references therein). Dynamic recrystallization processes such as subgrain rotation (SGR) and grain boundary migration (GBM) can also be associated with Dauphiné Twin (Lloyd, 2004; Neumann, 2000; Piazolo et al. 2005; Menegon et al. 2011; McGinn et al. 2020; Jaensch et al. 2022). Therefore, the interpretation of strain regime and deformation mechanism in polydeformed crustal rocks are far from straightforward, as different recrystallization mechanisms may operate at different *P-T* conditions on the same rock along with the possible effect of fluid infiltration, grain boundary sliding, recovery processes and also Dauphiné Twin. In this context, the LPO of recrystallized quartz grains may provide more insights into the deformation conditions of the final stage of exhumation/evolution of polydeformed rocks (Kohlstedt & Weathers, 1980; Hacker et al. 1992; Cross et al. 2015).

The Tso Morari Crystalline Complex (TMCC) of trans-Himalaya, eastern Ladakh, lies to the southwest of the Indo-Eurasian collisional suture zone (Figure 1) and consists of quartz, feldspar

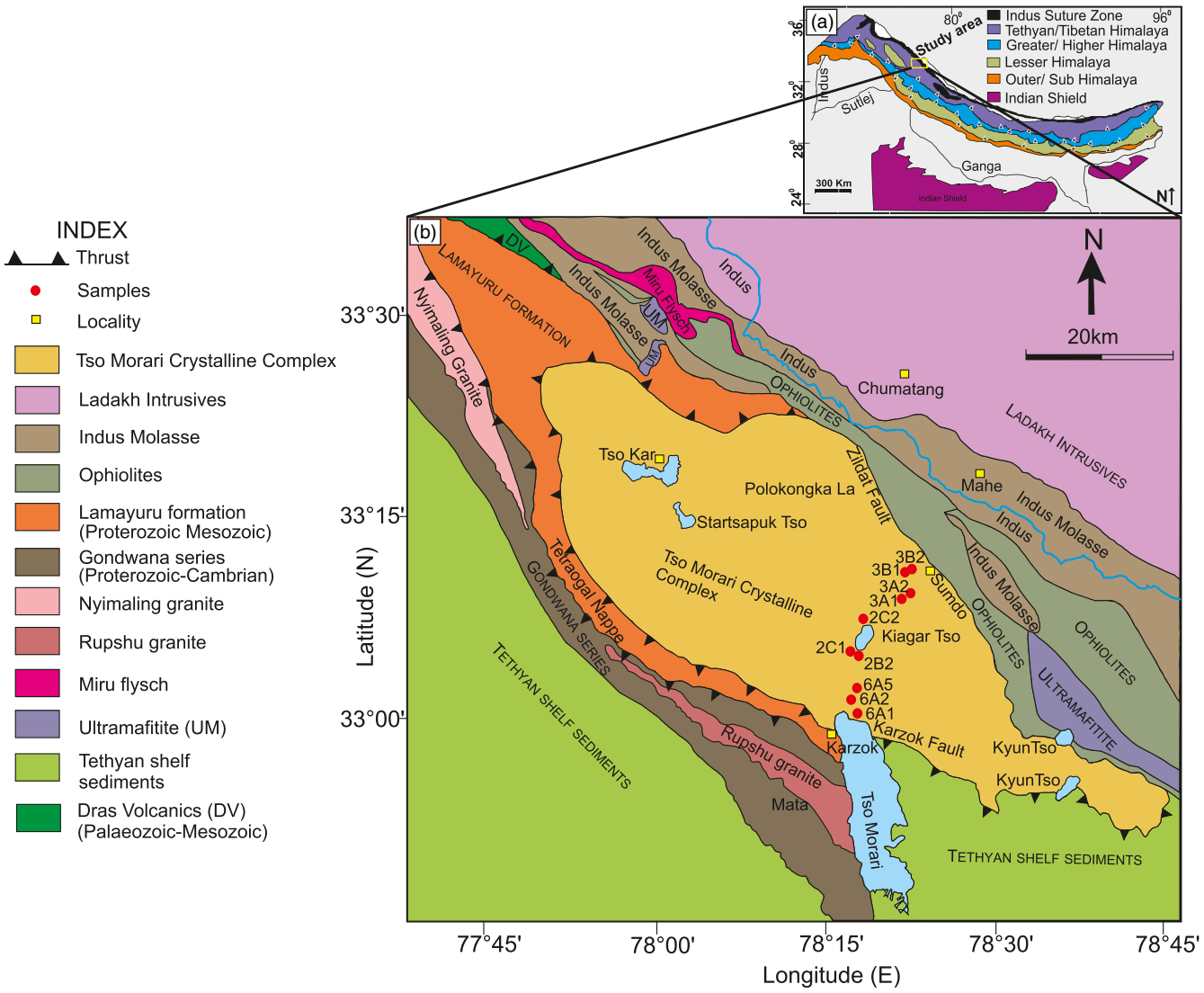

Figure 1. (Colour online) (a) Geological map of Himalaya and trans-Himalaya. The yellow box represents the present study area. (b) Geological map of the TMCC, N-W India (after Epard & Steck, 2008) showing major geological units and sample locations.

and mica-rich gneisses, locally called as the Puga Gneiss, with enclaves of metabasic rocks that underwent high to ultra-high pressure metamorphism during subduction of the north Indian continental margin (Steck et al. 1998; Guillot et al. 2000; de Sigoyer et al. 2000; Leech et al. 2005; Epard & Steck, 2008). Quartz LPO of the Puga Gneiss (Long et al. 2020; Dutta & Mukherjee, 2021) and omphacite and quartz from the metabasic enclaves (Dey et al. 2022) have been extensively studied in the recent past to understand the strain regime that prevailed during various stages of the tectonic evolution of the TMCC.

The objective of the present study is to understand the mechanism and regime of deformation that characterizes the retrogression stage and facilitates the final stage of exhumation of the TMCC (Puga Gneiss). In the present study, we have collected samples from the Puga Gneiss across the strike of the TMCC from the Zildat fault zone in the northeast to the Karzok fault zone to the southwest (Figure 1). For quartz LPO analysis by means of EBSD, we differentiated the relict quartz grains from the recrystallized ones of the Puga Gneiss on the basis of intragranular lattice distortion (Wheeler et al. 2009; Wright et al. 2011; Cross et al. 2017) and carried out LPO and misorientation analysis for both the suites of grains. Our analysis shows that the relict grains, in general, show multiple <c> axis maxima owing to signatures of different deformation events that occurred during the complex metamorphic evolution of the TMCC. On the other hand, the recrystallized grains, especially in the proximity of the binding fault zones of the TMCC, reflect simple shear or non-coaxial deformation. Our study helps infer that the LPO of relict quartz grains, for most samples, bears 'memory' of earlier deformation events and is difficult to interpret in terms of tectonic evolution of the TMCC. Contrary to this, misorientation analysis of the recrystallized grains indicates presence of Dauphiné Twin along with prism and rhomb <a>slip during recrystallization and grain size reduction. Furthermore, LPO of recrystallized quartz grains suggests that the final exhumation of the TMCC took place in a simple shear regime aided by activity along its two binding fault zones.

2. Geology of the area

The trans-Himalaya of eastern Ladakh is characterized by the NW-SE striking Indus Suture Zone (ISZ) that separates the Ladakh Magmatic Arc and the Indus Foreland sediments in the east of the

https://doi.org/10.1017/S0016756823000560 Published online by Cambridge University Press

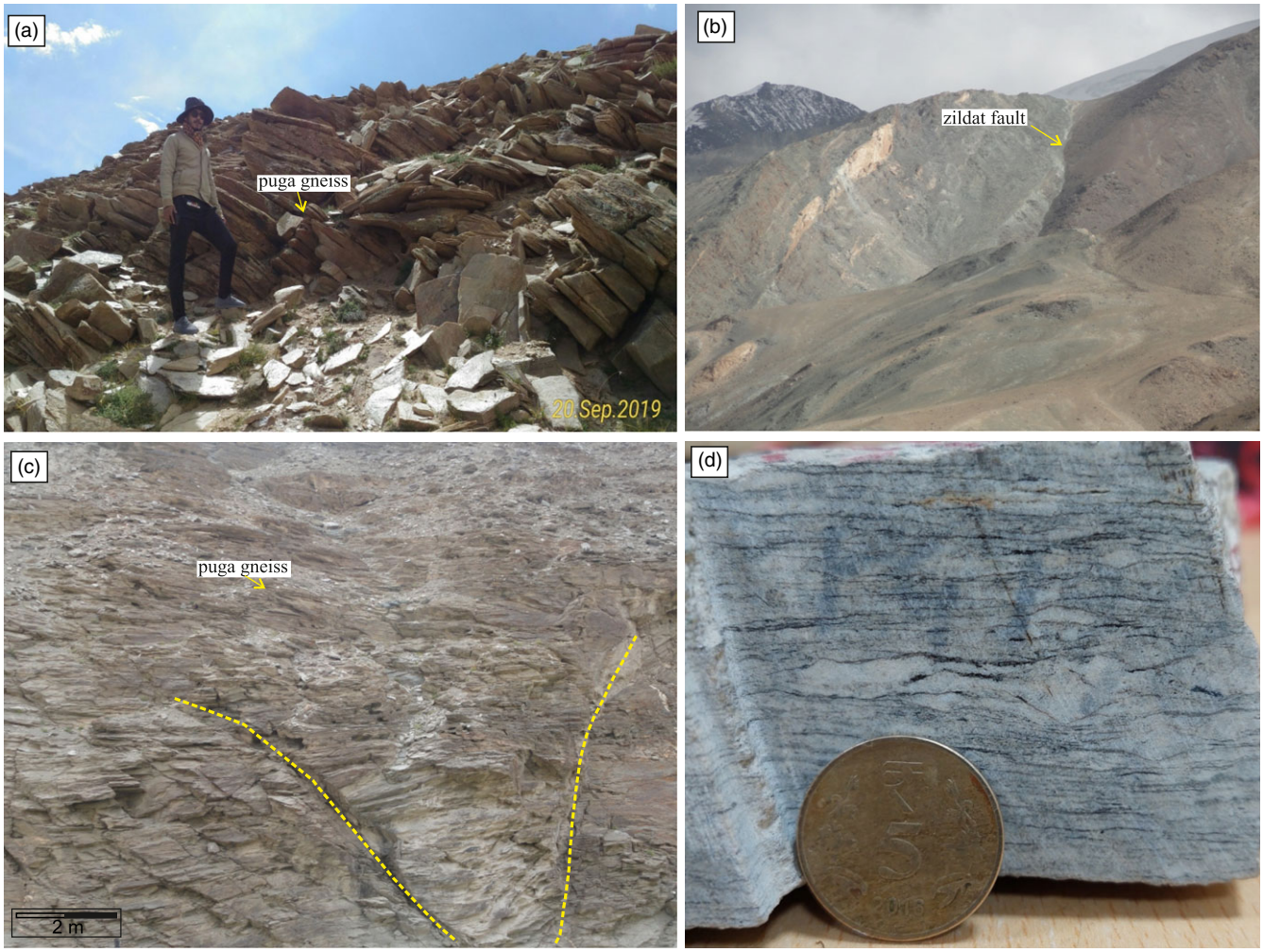

Figure 2. (Colour online) (a) Outcrop of granitic gneiss locally called Puga Gneiss (Location 6A2). (b) Outcrop showing the Zildat fault in Sumdo. (c) Outcrop of Puga Gneiss showing presence of conjugate fractures (Location 3B1). (d) A hand specimen of granitic gneiss cut parallel to XZ section showing asymmetric quartz porphyroclast (Sample 3A2); foliation bands are well developed and are comprised of muscovite.

ISZ from the ophiolite (Nidar Ophiolite) and ophiolitic mélanges (Zildat Ophiolitic Mélange) of Tethyan oceanic origin in the west of the ISZ (Figure 1; Thakur & Mishra, 1984). The TMCC lies to the west of the Zildat Ophiolitic Mélange. The Puga Gneiss, or its orthogneissic part, has a Cambro-Ordovician age (Figure 2a, c, d) (~479 Ma) (Girard & Bussy, 1999). The Zildat fault demarcates the boundary between the Zildat Ophiolitic Mélange and the TMCC (Figure 2b). In the western margin of the TMCC lies the Karzok fault, which separates the TMCC from the Paleozoic granites and Tethyan metasedimentary sequences (de Sigoyer et al. 1997; Hazarika et al. 2014, 2017). de Sigoyer et al. (2004) identified three deformation episodes in the TMCC. D1 phase of deformation (~55 Ma) is characterized by the formation of upright folds at eclogitic grade followed by the D2 deformation phase (~47 Ma), in dominantly garnet-amphibolite grade, during rapid exhumation that formed NW-SE trending open anticlines. The final D3 stage (~30 Ma) at the greenschist facies conditions is characterized by extensional movement along the Zildat and Karzok faults and is related to the final exhumation of the TMCC. Present-day movement along these two binding faults of the TMCC has also been observed through fault plane solutions of shallow crustal earthquakes of low to moderate magnitudes (Hazarika et al. 2017). Metamorphic modelling carried out by various workers on the eclogitic enclaves of the TMCC (e.g. St-Onge et al. 2014; Palin et al. 2017; review by O'Brien, 2019; Pan et al. 2020) suggests peak metamorphism at a *P-T* condition of ≥ 2.8 GPa and 550°C–650°C followed by near isothermal decompression up to 1 GPa and a subsequent high-temperature overprint (0.7–0.8 GPa and 680°C–720°C). This was followed by a clockwise path towards garnet-amphibolite, and finally, greenschist conditions (Figure 3). Study of Quartz LPO from the Puga Gneiss suggests exhumation of the TMCC through a combination of pure and simple shear (Long et al. 2020; Dutta & Mukherjee, 2021). EBSD analysis of omphacite and quartz carried out by Dey et al. (2022) on the eclogitic enclaves of TMCC also helped infer the transition from constrictional to plane strain during peak metamorphism to subsequent exhumation. Paul et al. (2017) carried out crustal anisotropy analysis based on shear wave splitting of both S-wave emanating from local earthquakes and P_S-converted phases of receiver function data. They observed fast polarizing direction parallel to the Zildat and Karzok faults of the TMCC.

3. Petrography and microstructures

The samples of Puga Gneiss collected for this study consist mainly of quartz, plagioclase, K-feldspar, muscovite and biotite. The ten

https://doi.org/10.1017/S0016756823000560 Published online by Cambridge University Press

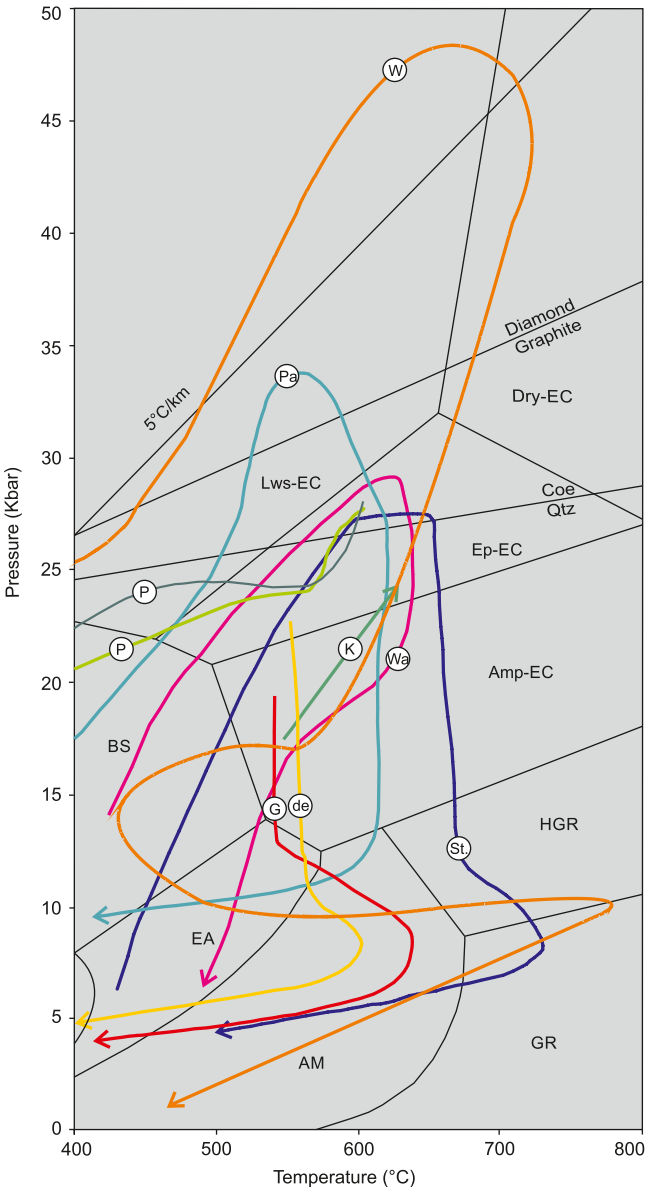

Figure 3. (Colour online) Diagram showing comparative *P-T* paths of Tso morari eclogite during its metamorphic evolution obtained by various workers (compiled and modified after Pan et al. 2020). The *P-T* paths compared are of (K) = Konrad-Schmolke et al. (2008); (St.) = St-Onge et al. (2013); (de) = de Sigoyer et al. (2000); (G) = Guillot et al. (1997); (Wa)= Warren et al. (2008); (W) = Wilke et al. (2015); (Pa) = Pan et al. (2020); (P) = Palin et al. 2017. Metamorphic facies boundaries are drawn after Gilotti (2013) and Hacker et al. (2013). Abbreviations of fields: Lws = Lawsonite; EC = Eclogite; Ep = Epidote; Amp = Amphibole; HGR = High-pressure Granulite; BS = Blueschist; GR = Granulite; EA = Epidote Amphibolite; AM = Amphibolite.

samples are divided into three zones on the basis of spatial distribution (Figure 1b). Samples 6A1, 6A2 and 6A5 are from the Karzok zone and are collected from the western part of the TMCC, near the Karzok fault. Samples 2B2, 2C1 and 2C2 are from the Kyeger Tso Lake region in the central part of the TMCC and samples 3A1, 3A2, 3B1 and 3B2 are from the eastern part of the TMCC or the Zildat fault zone. All the samples contain characteristic microstructures of both quartz and feldspar that develop at different ranges of temperature. Tectonic foliation in almost all the samples is defined by preferred orientation of muscovite and biotite. Quartz, along with feldspar, often shows a shape-preferred orientation parallel to this tectonic fabric. Samples from the Karzok zone show presence of plagioclase porphyroclasts surrounded by recrystallized quartzo-feldspathic aggregates (Figure 4a, b) forming 'core and mantle' microstructures, which is indicative of deformation at a relatively low temperature (Passchier & Trouw, 2005). Alternate layers of coarse- and fine-grained quartzo-feldspathic aggregates can be observed parallel to a tectonic fabric defined by shape preferred orientation of muscovite (Figure 4c). The central part of the TMCC also shows signs of deformation at a low temperature in the form of warping of muscovite around plagioclase porphyroclasts (Figure 4d). The plagioclase porphyroclast shows splaying fractures at high angle to the external foliation defined by muscovite. Bulging of quartz grain boundary into adjacent grain can also be observed (Figure 4e) along with presence of deformation twins in plagioclase (Figure 4f). The former is evidence of bulging recrystallization (BLG) and both these features are indicative of deformation at a comparatively low temperature, i.e. greenschist facies conditions. 'Pinning' of quartz grain by muscovite is also observed indicating GBM at a high temperature (Figure 4g) (Jessell, 1987; Stipp et al. 2002a; Passchier & Trouw, 2005). Prismatic subgrains with varying extinction angles were observed within single quartz grains (Figure 4h), indicating the activation of multiple slip systems during a recovery process or SGR. Quartz also shows presence of sutured grain boundaries and presence of small sub-rounded recrystallized grains (Figure 4g, h) indicating GBM. GBM is also observed in samples from the Zildat fault zone in the form of sutured grain boundaries in quartz having varied grain sizes (Figure 4i) along with presence of 120° triple junctions (Figure 4j). Overall, our microstructural observations suggest dynamic recovery and recrystallization at high temperature (> 550°C) (GBM of quartz; Stipp et al. 2002a, b; pinning and dragging microstructure) and medium to high temperature (400°C–550°C) as evidenced by presence of prismatic subgrains in quartz or SGR in quartz (Stipp et al. 2002a, b) and also by the presence of recrystallized grains and irregular grain boundaries of plagioclase and K-feldspar (Tullis & Yund, 1985, 1987). Microstructures developed at low temperatures (< 400°C) (BLG in quartz; Stipp et al. 2002a, b and deformation twin in plagioclase; Tullis & Yund, 1985) are also common.

4. Analytical techniques

Measurement of quartz LPO was the critical analysis to be performed in this study. For this, SEM-EBSD analysis was done on Broad Ion Beam (BIB) polished rock thin sections. BIB polishing was done following the MFAL protocol of Mamtani et al. (2020). Slides were initially polished with colloidal silica, followed by BIB polishing, consisting of two steps: 5 minutes of surface cleaning followed by 30 minutes of polishing. EBSD patterns were acquired at 30 kV accelerating voltage, 1.49 x 10^{-6} mbar system vacuum, and ~15 mm working distance using Carl Zeiss Auriga Compact FEG-SEM fitted with NordlysMax2 EBSD detector (Oxford Instruments, UK) in Indian Institute of Technology Kharagpur (India). Thin sections were placed in the SEM sample chamber and tilted to 70° before the EBSD analyses. Data acquisition and indexing of EBSD patterns were carried out automatically using Aztec software (Oxford Instruments, UK), along with the elimination of wild spikes. Step size in the range of 6–7.5 μm was taken for EBSD mapping. Grain size distribution, grain-orientation spread (GOS) (Figure 5), distribution of misorientation angles of quartz and axis/angle misorientation distribution analyses were carried out using MTEX 5.7.0., an open-source MATLAB toolbox for quantitative texture analyses, available at

https://doi.org/10.1017/S0016756823000560 Published online by Cambridge University Press

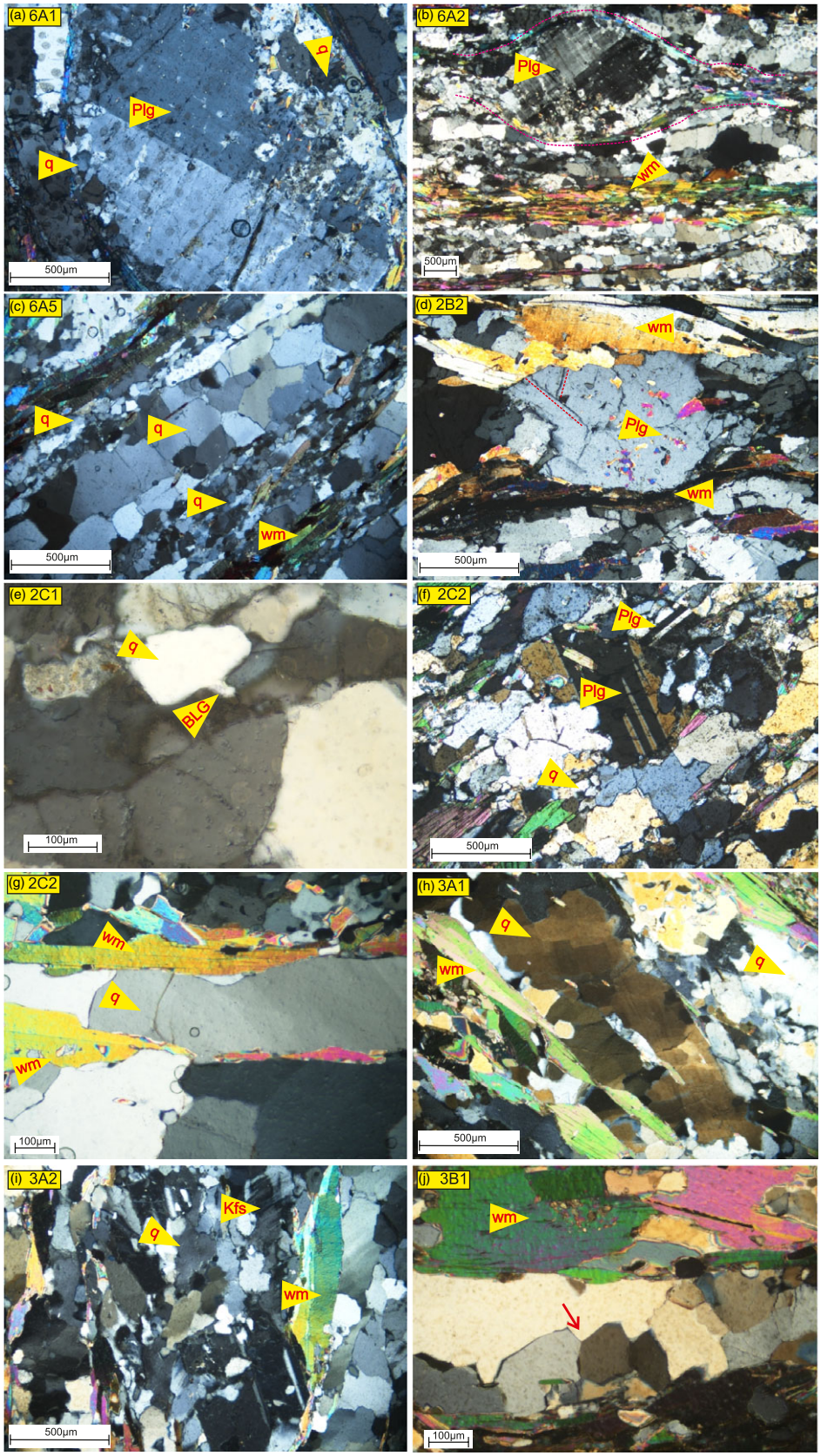

Figure 4. (Colour online) Photomicrographs showing microstructural features from the Puga Gneiss (a) Twinned plagioclase porphyroclast surrounded by recrystallized quartzo-feldspathic aggregate forming 'core and mantle' structure. (b) Warping of thin film of white mica-rich aggregate around a plagioclase porphyroclast. Note presence of quartzo-feldspathic aggregate in the 'pressure shadow' zone and also strong tectonic foliation defined by preferred orientation of white mica. (c) Alternate layers of fine- and coarse-grained quartzo-feldspathic aggregates lying parallel to the tectonic foliation. (d) Warping of foliation defined by biotite and muscovite around a plagioclase porphyroclast. Note splaying microfractures (marked by red dotted lines) within the porphyroclast at a high angle to the external foliation. (e) Bulging of quartz grain boundary in the adjacent grain. (f) Deformation/tapered twins in plagioclase. Note evidence of GBM in plagioclase and quartz in the form of highly irregular grain boundaries and presence of sub-rounded recrystallized grains. (g) 'Pinning' of quartz grain by muscovite. (h) Prismatic subgrains of quartz lie concordant with the tectonic foliation defined by mica flakes. (i) Highly irregular/sutured grain boundaries in recrystallized quartz and K-feldspar suggesting grain boundary migration (GBM). (j) Formation of 120° triple junction in quartz owing to GBM. Mineral abbreviations: q = Quartz; Plg = Plagioclase; wm = Muscovite; Kfs = K-Feldspar.

https://doi.org/10.1017/S0016756823000560 Published online by Cambridge University Press

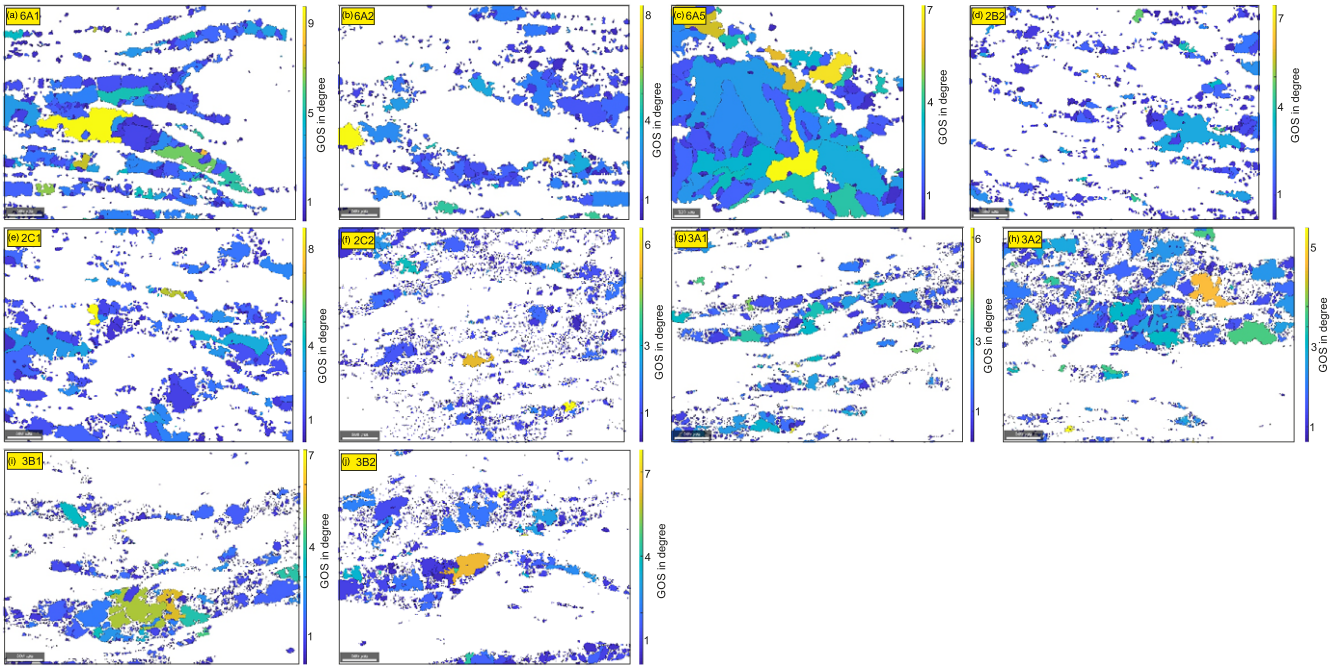

Figure 5. (Colour online) Grain orientation spread (GOS) map of quartz for all the samples. All grains < 100 μm in size and with < 2.5° GOS are recrystallized grains and rest are relict grains.

http://mtex-toolbox.github.io (Hielscher & Schaeben, 2008). A 10° threshold angle was used for grain segmentation, keeping only grains that are bigger than 5 μm in size (area of the grain) and have more than three orientation solutions. Grain boundaries are also smoothened. Halfwidth of 10° was kept. Pole figures were plotted using one point per grain to avoid oversampling bias of large porphyroclastic grains. Grains separated by 60±5° rotation around the <c> axis, or Dauphiné twin boundaries (Figure 6), were merged before pole figure analysis. The cylindricity index (B) (Vollmer, 1990) was used to characterize the distribution of quartz c-axes. B ranges between 0 and 1, starting from completely random fabric to a completely nonrandom fabric. B represents the sum of the point (P) and girdle (G) end-member fabric components. Fabric strength of the indexed phases was calculated using the M-index (Skemer et al. 2006). The M-index is defined as:

$$M = \frac{1}{2}\int \mathrm{IR}^{\mathrm{T}}(\theta) - \mathrm{R}^{0}(\theta)|\mathrm{d}\theta$$

Where $R^T(\theta)$ is the theoretical distribution of misorientation angle for a random fabric, and $R^0(\theta)$ is the distribution for observed misorientation angles. All the pole figures are plotted after determining the vorticity normal surface (VNS). A ratio of 1: 4 for magnitude of principal and secondary axes of each grain scale dispersion was kept as a threshold to ignore analyzed points with insignificant dispersion of lattice (https://github.com/zmichels/CVA). The VNS was determined using the crystallographic vorticity analysis (CVA) using MTEX, following the method of Michels et al. (2015) and Giorgis et al. (2017).

Recrystallized and relict quartz grains were differentiated and treated separately for LPO analysis. The characterization of recrystallized and relict grains was carried out following the method outlined by Cross et al. (2017). This method distinguishes recrystallized grains on the basis of GOS that reflects intracrystalline lattice distortion. The GOS threshold (2.5°) for classification is determined by identifying the knee of the trade-off curve of GOS and cumulative grain counting of each dataset (Cross et al. 2017). Differential flow stress was also calculated for all indexed quartz grains having a size < 100 μm using the quartz piezometer of Stipp & Tullis (2003). The mean grain size (area of the grain) values for the recrystallized grains are given as root mean square values of circle equivalent diameters (Cross et al. 2017).

The piezometer relationship (Stipp & Tullis, 2003) is:

$$D = 10^{3.56\pm0.27} * \sigma^{-1.26\pm0.13}$$

Where D is the mean diameter and σ is differential flow stress.

It may be noted that number of grains considered for differential stress analysis and LPO analysis are different, as for LPO analysis of recrystallized quartz grains, apart from having a size of < 100 μm, only grains having GOS < 2.5° and size > 5 μm are considered.

5. Results

5.1. Quartz grain size distribution and differential stress estimation

Quartz grain size distribution for both relict and recrystallized grains are shown in Figure 7 and Figure 8 and Table. 1. In the Karzok zone, mean relict grain size varies from 90.78 μm (Sample No. 6A2) to 109.48 μm (Sample No. 6A1). For recrystallized grains, the average size varies from 4.60 μm (Sample No. 6A2) to 6.51 μm (Sample No. 6A5). In the Central zone, the mean relict grain size varies from 101.01 μm (Sample No. 2B2) to 354 μm (Sample No.2C1). Mean recrystallized grain size varies from 3.29 μm (Sample No. 2C2) to 5.17 μm (Sample No. 2B2). In the Zildat zone, the mean relict grain size ranges from 280 μm (Sample No. 3A1) to 618.58 μm (Sample No. 3A2). The mean size of recrystallized grains from this zone varies from 3.03 μm (Sample No. 3B2) to 4.15 μm (Sample No. 3A1). Differential stress values obtained from the

https://doi.org/10.1017/S0016756823000560 Published online by Cambridge University Press

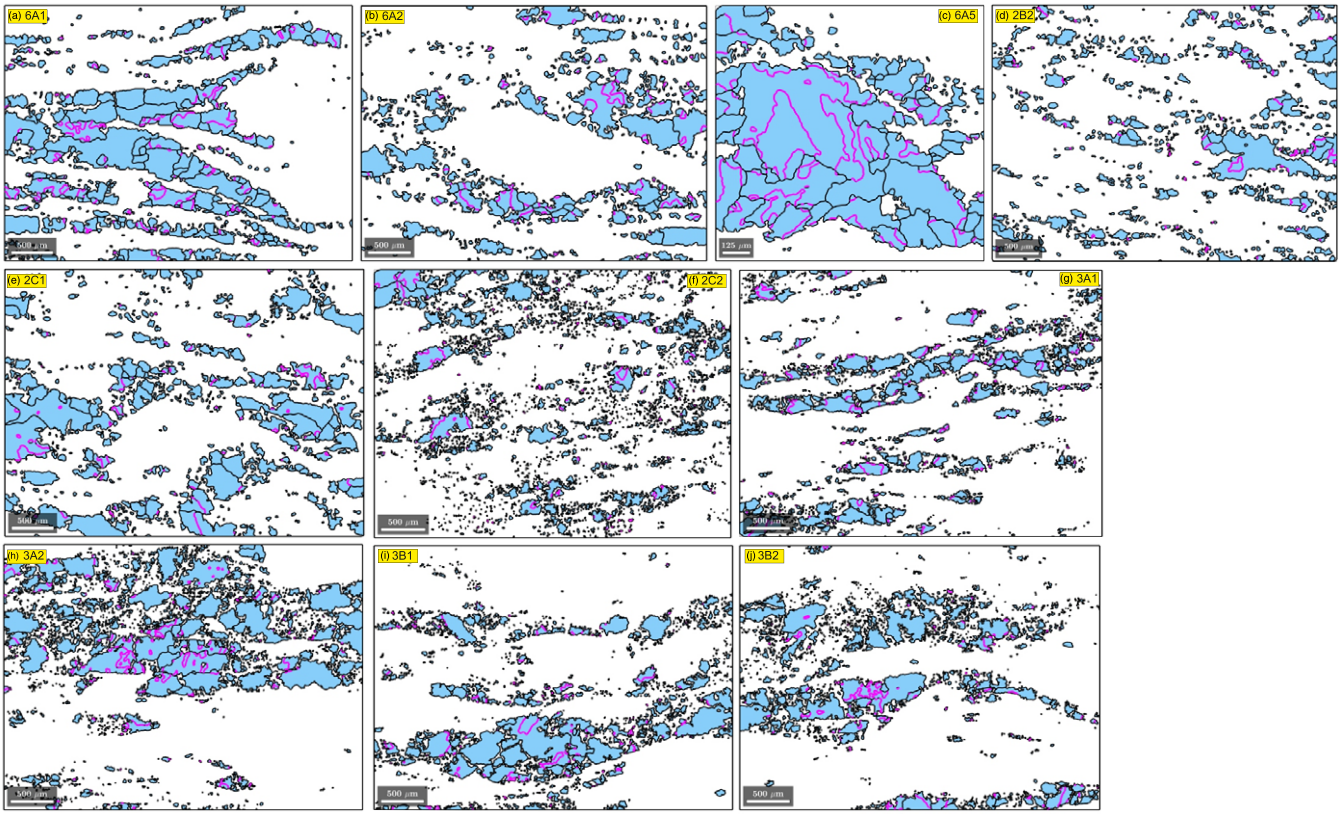

Figure 6. (Colour online) Quartz phase map showing presence of Dauphiné twin boundaries marked by magenta lines.

Karzok zone vary from 80.07 MPa (Sample No. 6A5) to 104.77 MPa (Sample No. 6A2). In the Central zone, it varies from 97.83 MPa (Sample No. 2C1) to 115.83 MPa (Sample No. 2C2). In the Zildat zone, the differential stress values are slightly higher with minimum value of 103.5 MPa (Sample No. 3A1) to 122.61 MPa (Sample No. 3B2). It may be noted that sample 3B2 lying closest to the Zildat fault shows recrystallized grains whose mean size indicates the highest value of differential stress. (Table. 1).

5.2. LPO of Quartz

As evident from past metamorphic modelling studies (Figure 3), the TMCC has experienced a complex metamorphic history and it is likely that its quartz grains have experienced multiple deformations starting from peak metamorphism to exhumation to high-temperature overprint and finally retrogression till greenschist facies conditions. This implies that the analyzed samples may show LPO patterns regarding different *P-T* conditions by the activation of different slip systems. Therefore, relict (GOS > 2.5°) and recrystallized (GOS < 2.5°) grains are treated separately to infer any meaningful LPO and active slip systems during the late retrogression or the final exhumation stage of these rocks. Keeping this in mind, pole figures were prepared separately for relict and recrystallized grains for all ten samples. The M and B indices for the relict grains vary from 0.0336 to 0.1525 and 0.1950 to 0.6653, respectively (Table 1). For the recrystallized grains, these indices are much lower, and they vary respectively from 0.0110 to 0.0933 and 0.1927 to 0.5533 (Table 1). Maximum values multiple uniform distribution were calculated based on one point per grain of the <c> axis and it varies from zero to six for relict grains and from zero to five for recrystallized grains. All other crystallographic axes and planes have maxima lower than that of the <c> axis.

5.2.1. Karzok zone

<c> axis plot of relict grains from sample 6A1 shows one strong maxima lying in the NE quadrant of the pole figure and two weaker maxima showing a polar distribution in the NW and SE quadrant lying oblique to the XZ plane (Figure 9a, b). Apart from the <c> axis, only the negative rhomb z {01-11} shows partial girdle distribution parallel to the foliation plane for this sample. 6A2 shows a strong <c> axis maxima at ~10° anticlockwise from the Y-axis in the southern quadrant. A weaker maxima showing polar distribution at opposite quadrants can also be seen lying ~20° anticlockwise from the lineation (Figure 9c). 6A5 also shows multiple <c> axis maxima with the strongest lying in the NW quadrant and defining a polar distribution at ~10° anticlockwise from the Y-axis. Other maxima can also be observed at the southern quadrant (Figure 9d). The recrystallized grains show a more regular pattern of <c> axis distribution in the pole Figure 6A1 shows single girdle distribution ~10° counterclockwise from the XZ plane (Figure 10a). Both 6A2 and 6A5 show strong maxima at ~10° clockwise from the Y-axis (Figure 10b, c). The a-axis <11–20> shows weak girdle distribution along the foliation plane for sample 6A5 (Figure 10c).

5.2.2. Central zone

Relict grains from both samples 2B2 and 2C1 show irregular distribution with multiple maxima for <c> axis (Figure 9e, f). Only sample 2C2 shows strong polar distribution of <c> axis along the

https://doi.org/10.1017/S0016756823000560 Published online by Cambridge University Press

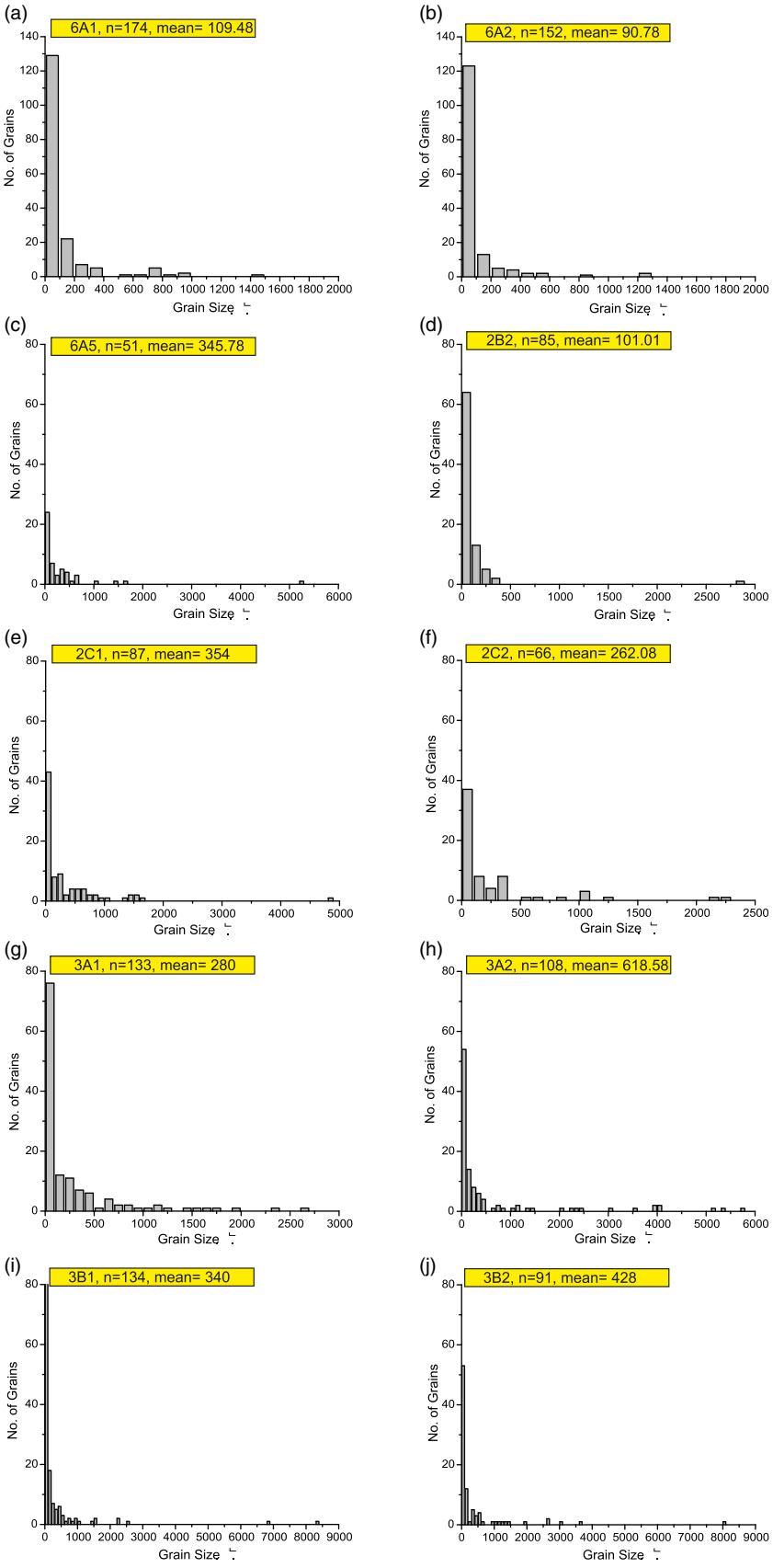

Figure 7. (Colour online) Histograms showing grain size distribution of relict quartz grains for all the samples. The X-axis varies according to the size of the largest grain and y-axis according to the number of grains of certain size.

https://doi.org/10.1017/S0016756823000560 Published online by Cambridge University Press

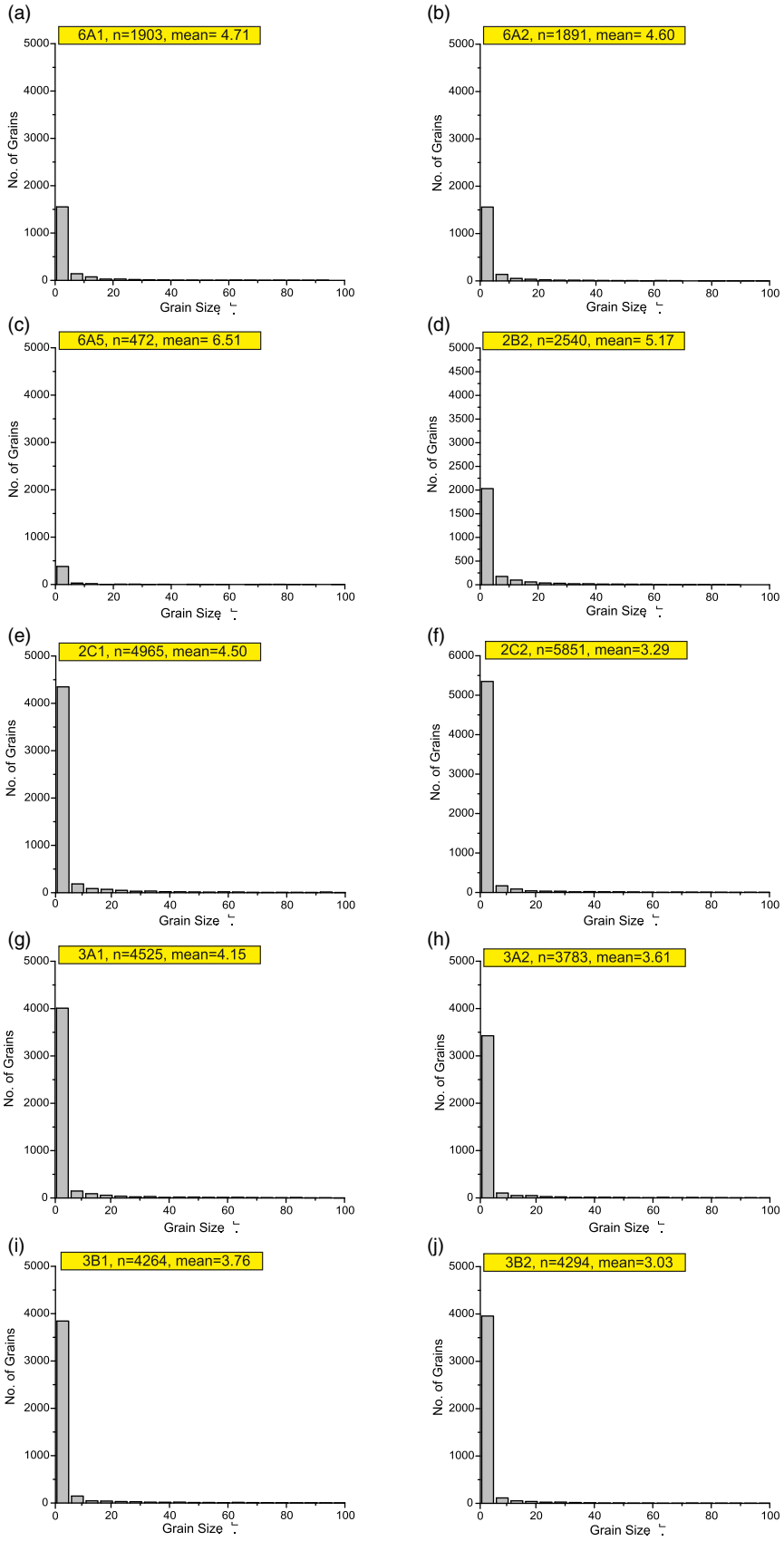

Figure 8. (Colour online) Histograms showing grain size distribution of recrystallized quartz grains for all the samples. Y-axis varies according to the number of grains of certain size.

https://doi.org/10.1017/S0016756823000560 Published online by Cambridge University Press

Table. 1. Table showing total number of relict and recrystallized quartz and also number of recrystallized grains used for LPO analysis

Sample No.	N_{Relict} (Grain size > 5μ; GOS > 2.5°)	$N_{Differential\ Stress}$ (Grain size < 100μ; GOS < 2.5°)	$N_{Recrystallized}$ (Grain size > 5 μ and < 100μ; GOS< 2.5°)	Differential stress value (in MPa)	Relict grains		Recrystallized grains	
					B-index	M-index	B-index	M-index
6A1	66	1903	441	102.39	0.5051	0.1170	0.4870	0.0443
6A2	37	1891	406	104.77	0.5089	0.1225	0.4522	0.0366
6A5	46	472	97	80.07	0.6653	0.1170	0.2991	0.0492
2B2	41	2540	513	100.131	0.4677	0.1186	0.3674	0.0202
2C1	144	4965	735	97.83	0.3383	0.0345	0.3841	0.0585
2C2	108	5851	586	115.83	0.4547	0.0855	0.3725	0.0808
3A1	142	4525	620	103.5	0.1950	0.0336	0.1927	0.0110
3A2	134	3783	445	109.11	0.6171	0.1525	0.4443	0.0670
3B1	117	4264	484	107.09	0.4858	0.0739	0.3606	0.0255
3B2	109	4294	445	122.61	0.4579	0.0511	0.5533	0.0933

B and M index for relict and recrystallized grains for all the samples are also shown. Note that the number of recrystallized grains shown for differential stress estimation and pole figure analysis are different as for the former all grains having grain size < 100 μ and GOS< 2.5° are considered while for pole figure analysis using CVA grains < 5 μ and GOS< 1° are also excluded. Similarly, the number of relict grains shown in histogram in Figure 7 and those used for pole figure analysis are different as all relict grains having GOS > 2.5° are considered for histogram but only grains bigger than 5 μ are considered for pole figure analysis. Apart from that, for pole figure analysis of both relict and recrystallized grains, a ratio of 1:4 for magnitude of principal and secondary axes of each grain scale dispersion was kept as a threshold for CVA analysis.

Y-axis and one secondary maxima lying on the Z-axis (Figure 9g). Recrystallized grains from 2B2 and 2C2 show <c> axis maxima lying sub-horizontally ~5° anticlockwise from the XZ plane (Figure 10d, f). 2C1 shows strong <c> axis maxima lying on the z-axis (Figure 10e) indicating prism <a> slip.

5.2.3. Zildat zone

In this zone, relict grains from sample 3A1 show <c> axis maxima at the southern quadrant lying ~10° clockwise from the Y-axis. A weak girdle parallel to the XZ plane can also be observed (Figure 9h). Samples 3A2 and 3B2 show strong <c> axis maxima defining an asymmetric single girdle at a high angle to the foliation plane (Figure 9i, k). On the other hand, 3B1 shows strong <c> axis maxima lying on the Z-axis and a weaker maxima defining weak girdle distribution along the Y-axis (Figure 9j) indicating both prism and rhomb <a> slip components. Recrystallized quartz grains of 3A1 show <c> axis point maxima lying at opposite quadrants at ~45° anticlockwise from the XZ plane (Figure 10g). 3A2 has <c> axis point maxima slightly off centre to the Z-axis and defines a weak girdle ~45° anticlockwise from the XZ plane (Figure 10h). 3B1, on the other hand, shows <c> axis maxima lying subparallel to the XZ plane defining a girdle distribution (Figure 10i). For sample 3B2, the <c> axis has a single asymmetric girdle distribution lying ~5° anticlockwise from the Y-axis (Figure 10j).

5.3. Quartz misorientation

Misorientation angle distribution for the relict and recrystallized quartz grains are shown in Figure 11 and Figure 12. Both the correlated (misorientation between neighbouring grains) and uncorrelated (misorientation between random grains far from each other) are shown. It can be observed that in case of the relict grains from majority of the samples, the misorientation angle frequency varies from the theoretical uniform distribution (green curve). On the other hand, in case of the recrystallized grains, frequency of misorientation and the theoretical uniform distribution curve match almost perfectly. For the relict grains of samples 6A1 and 6A5, a misorientation angle frequency peak can be observed at 60° (Figure 11a, c). The misorientation axis/angle pair inverse pole figures shown in crystal coordinates reveal that this misorientation angle frequency lies parallel to the <c> axis (Figure 12b, d). In fact, integration of the misorientation angle distribution with the corresponding axis/angle pair inverse pole figure reveals that the frequency of misorientation angle observed at 60° interval lies invariably parallel to the <c> axis for all the samples (Figure 11 and Figure 13). The high-angle misorientations (≥70°) are generally parallel to the <z> and <r> plane with sample 6A2 showing high-angle misorientation parallel to the <a> axis (Figure 13). Relict grains from all the samples except 2C1 show low-angle (≤15°) misorientation parallel to the <c> axis. 2C1 shows low-angle misorientation parallel to the <a> axis. For the intermediate ranges of misorientation angles (15° to 55°), the axis/angle pair inverse pole figures show multiple point maxima that indicate activation of multiple slip systems (Figure 13). Only sample 2C1 shows misorientation angles in the range of 15° to 35° and 35° to 55° lying parallel to the <a> and <c> axes, respectively. For the recrystallized grains, both the low angle (≤15°) and 60±5° misorientation angles lie parallel to the <c> axis (Figure 12 and Figure 14). In the recrystallized grains, misorientation around 60° is the only major frequency peak observed (Figure 12).

6. Discussion

Before we interpret the petrographic and EBSD results obtained from both relict and recrystallized quartz grains, it is necessary to understand the conditions at which the microstructures and LPO of quartz may have developed. As mentioned earlier, the TMCC has a complex metamorphic history (Figure 3), and it is very likely that the relict quartz grains, in particular, may reflect microstructures developed during UHP, decompression or high-temperature overprint episodes of metamorphism (Figure 3). Our petrographic observations (Figure 4) suggest that the Puga

https://doi.org/10.1017/S0016756823000560 Published online by Cambridge University Press

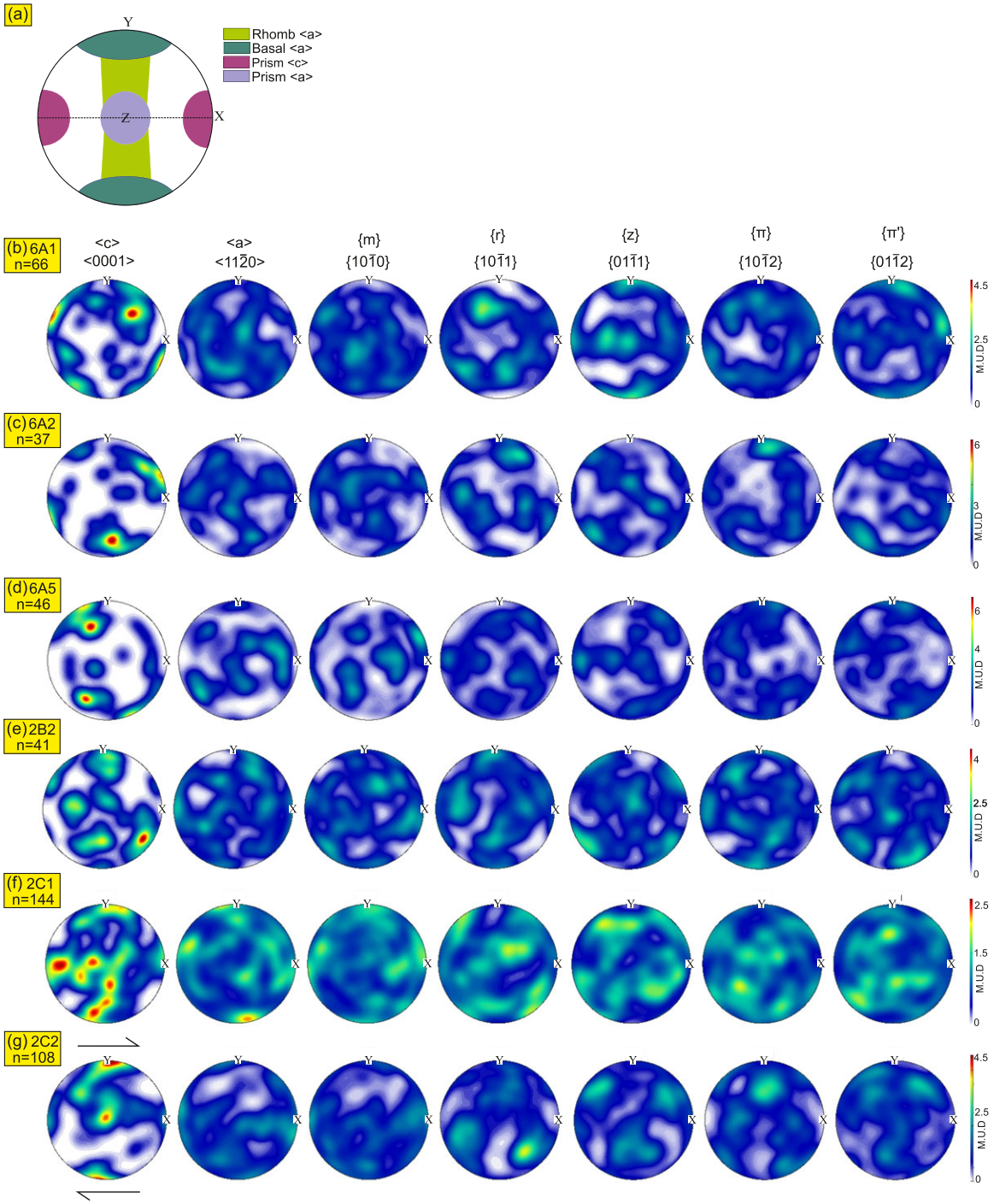

Figure 9. (Colour online) (a) Cartoon showing plotting conventions for inferences of quartz slip systems (after Neumann, 2000). (b–k) Quartz LPOs shown in lower hemisphere equal-area projections (halfwidth = 10°) for relict quartz grains for all the samples. Shear senses are marked for samples having asymmetric single girdle or polar distribution oblique to foliation for the <c> axis.

Gneiss bears signature of recovery and recrystallization at a high temperature (GBM at > 500°C) in the form of 'pinning' (Figure 4g) and GBM microstructures (Figure 4i), 120° triple junctions and irregular grain boundaries in quartz (Figure 4j) along with evidences of SGR including prismatic subgrains in quartz (Figure 4h) indicating recovery and recrystallization in a temperature range of 400°C–550°C (Stipp et al. 2002b). Furthermore, BLG in quartz (Figure 4e), deformed twins in plagioclase (Figure 4f) and presence of fine-grained quartzo-feldspathic aggregate parallel to the tectonic foliation (Figure 4c) may have developed at a lower temperature range of 270°C–400°C (Tullis & Yund, 1985; Stipp et al. 2002a, b; Passchier & Trouw, 2005). These observations would suggest that the Puga Gneiss developed microstructure and LPO during the clockwise *P-T* evolution (Figure 3) of the TMCC with continued exhumation, retrogression and progressive lowering of temperature. Dutta & Mukherjee (2021) carried out

https://doi.org/10.1017/S0016756823000560 Published online by Cambridge University Press

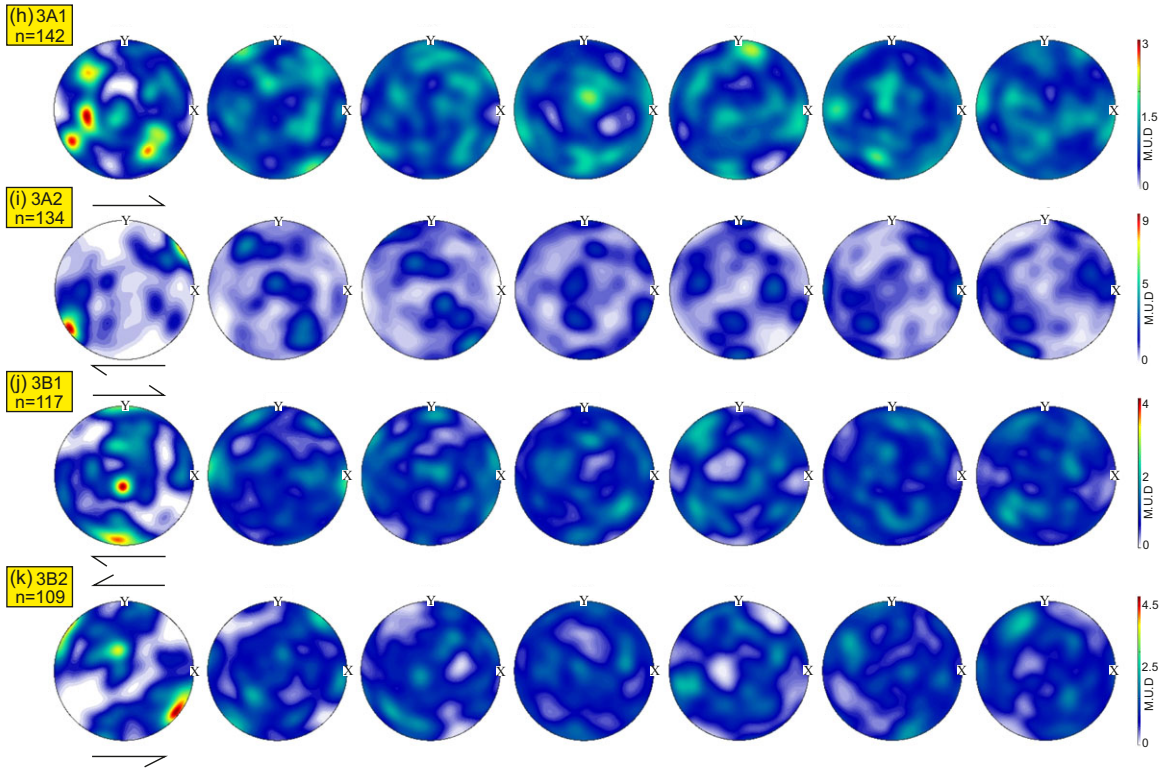

Figure 9. (Continued).

detailed microstructural analysis of the Puga Gneiss and inferred a deformation temperature range starting from < 400°C to > 600°C. The study by Long et al. (2020) on the Puga Gneiss suggests deformation temperature ranging from 330°C to 600°C. Our temperature estimates, based on published pseudosection modelling (Figure 3) and our microstructural observations, have a similar range of temperature. However, we infer a temperature range of ~270°C to ≥ 550°C for deformation and development of microstructures (BLG to GBM regime of dynamic recovery and recrystallization of quartz).

It may be noted that, apart from quartz, plagioclase and muscovite are the two major constituent minerals observed in the studied samples. The relationship between these rheologically different minerals with quartz, in terms of deformation, needs to be taken into account to understand the microstructural evolution of the studied rocks. As described earlier, both plagioclase and quartz show characteristic recovery and recrystallization microstructures developed at high temperature and at intermediate temperature to low-temperature conditions. However, some amount of strain partitioning can be envisaged between these two phases, as some of the plagioclase porphyroclasts are not completely disaggregated and retain their lens-like shape (Figure 4d) and even subhedral shape (Figure 4f). This indicates rheological competence of plagioclase in comparison to quartz. It can be argued that presence of rheologically stronger feldspar and weaker quartz may have caused strain partitioning with the non-coaxial strain accommodated by the weaker phase in the matrix, i.e. quartz-rich fine-grained layers, and coaxial shear partitioned in the more competent feldspar porphyroclasts (Lister & Williams, 1983). Presence of splaying microfractures within the plagioclase porphyroclasts, lying at a high angle to the external foliation (Figure 4d), can be inferred to be a result of partitioning of strain in coaxial shear component within the porphyroclast and non-coaxial shear component within the external foliation. Experimental study by Holyoke & Tullis (2006) suggests that muscovite is a much weaker phase than quartz and plagioclase. In the Puga Gneiss, muscovite generally defines the tectonic foliation by preferred orientation and, sometimes, shows monoclinic shape (Figure 4g–j). Muscovite, apart from developing 'pinning' microstructures at relatively higher temperature (Figure 4g), generally recorded the latest deformation episode at a relatively low temperature that coincides with the timing of development of strong tectonic fabric, along which they are usually aligned. However, presence of 'pinning' of quartz indicates that GBM of quartz has been controlled by mica to some extent.

Dauphiné twinning reverses the positive and negative crystallographic forms of α-quartz through a 60° rotation around the <c> axis. It exchanges the positive and negative rhombs and <a> directions without changing the <c> axis (Thomas & Wooster, 1951; Tullis & Tullis, 1972; Rahl et al. 2018). With the advent of EBSD, Dauphiné twinning has been recognized in various geological conditions in quartz-bearing metamorphic rocks (Menegon et al. 2011 and references therein). Studies have shown that Dauphiné twinning plays an important role in intracrystalline plastic deformation in quartz (Menegon et al. 2011) and there is an intricate relationship between Dauphiné twinning, microstructural modifications and development of shear bands in quartz-bearing rocks (Neumann, 2000; Lloyd, 2004; Piazolo et al. 2005; Menegon et al. 2011; Morales et al. 2011; McGinn et al. 2020; Jaensch et al. 2022). According to Lloyd (2004), Dauphiné twinning assists in progressive grain size reduction along with formation of new grains and subgrain boundaries. According to Stipp & Kunze (2008), Dauphiné twins are preferred sites for dynamic recrystallization. Recent studies by McGinn et al. (2020) and Jaensch et al.

https://doi.org/10.1017/S0016756823000560 Published online by Cambridge University Press

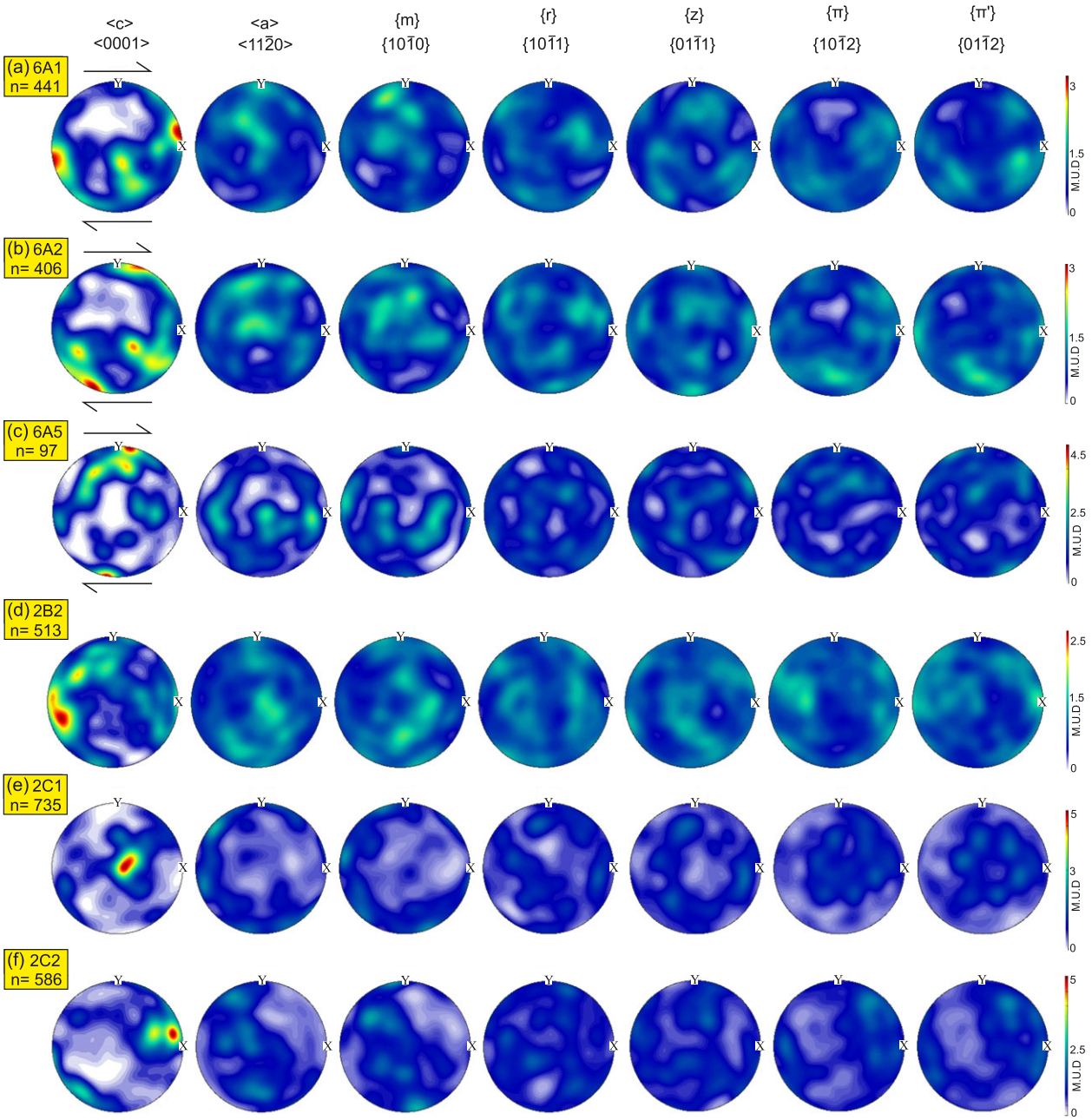

Figure 10. (Colour online) (a–j) Quartz LPOs shown in lower hemisphere equal-area projections (halfwidth = 10°) for recrystallized quartz grains for all the samples. Shear senses are marked for samples having asymmetric single girdle or polar distribution oblique to foliation for the <c> axis.

(2022) also highlighted the importance of Dauphiné twinning in accommodation and localization of strain. Dauphiné twinning reduces the stiffness of the quartz crystal and converts it into a more deformable object (Tullis, 1970). Experimental study carried out by Wenk et al. (2007) suggests that a minimum temperature of 300°C–400°C is required for Dauphiné twins to occur with a differential stress of at least ~ 100 MPa. Past studies have reported occurrence of Dauphiné twins in SGR regime (Lloyd, 2004; Menegon et al. 2011; Morales et al. 2011) as well as in GBM regime (Neumann, 2000; Piazolo et al. 2005; McGinn et al. 2020). Piazolo et al. (2005) reported Dauphiné twins related to α-β transition in quartz, which occurs at granulite-grade temperatures. On the other hand, Jaensch et al. (2022) have reported Dauphiné twins in folded conglomerate deformed in greenschist facies conditions. This suggests that Dauphiné twinning in quartz can occur at wide ranges of metamorphic conditions.

Twin boundaries that are at 60° angle to the <c> axis are plotted on the quartz phase map that reveals presence of Dauphiné twins (Figure 6). Misorientation analysis of relict quartz grains from all samples, except 2C2 and 3B1, shows a prominent frequency peak at 60°, which is the highest for samples 6A1 and 6A5 (Figure 11). This may suggest presence of Dauphiné twins. However, frequency distribution of misorientation angles should not be the only criteria to identify Dauphiné twin. The misorientation angle, in case of a Dauphiné twin, must be aligned with misorientation axis parallel to the <c> axis (Lloyd, 2004). Misorientation axis/angle pair

https://doi.org/10.1017/S0016756823000560 Published online by Cambridge University Press

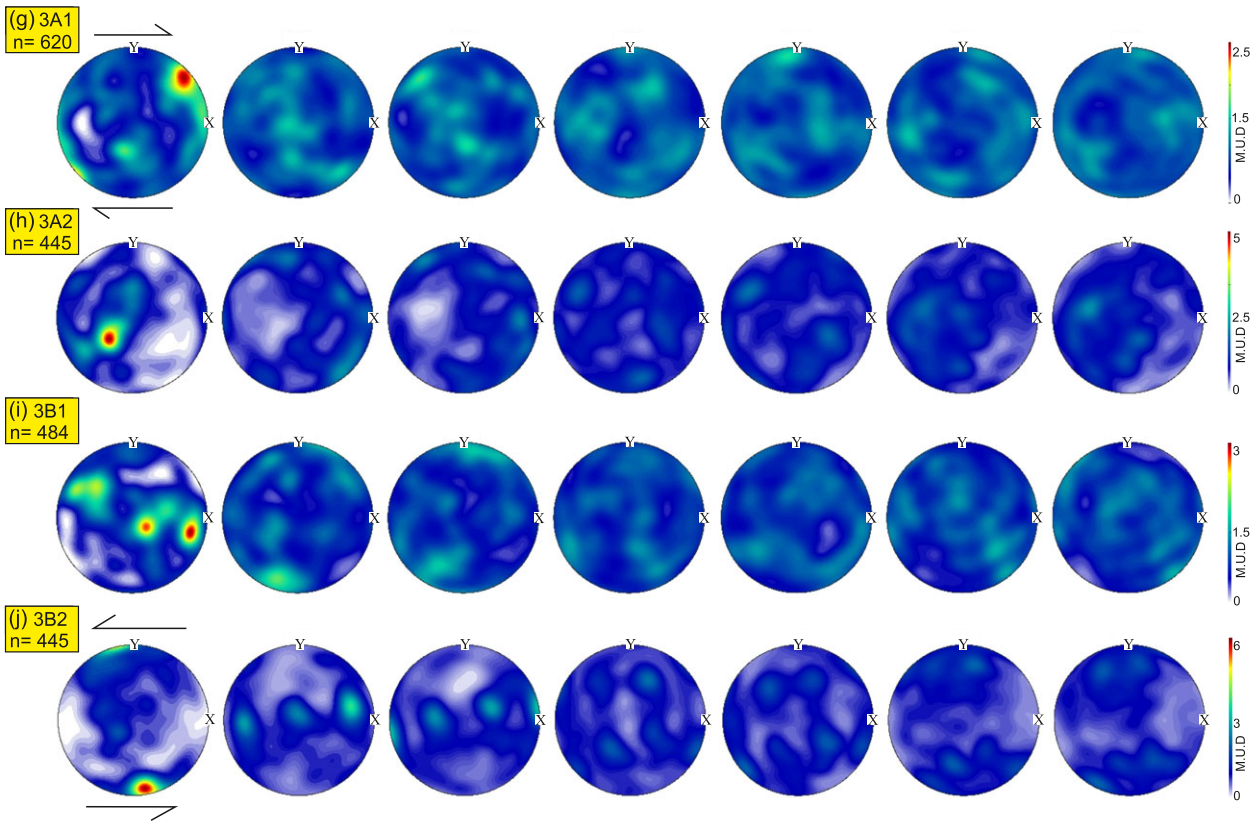

Figure 10. (Continued).

analysis (Figure 12) clearly shows that the dominant 60° misorientation angle is parallel to the <c> axis. In brief, for the relict quartz grains, the misorientation axis/angle analysis shows that the low angle (2° to 15°) and for angles around 60°, the misorientation angle is aligned parallel to the <c> axis. The preferred alignment in case of 60°±5° confirms the presence of Dauphiné twins. On the other hand, recrystallized grains from all the samples show a prominent frequency peak at 60° (Figure 12), which lies parallel to the <c> axis (Figure 14) and indicates presence of Dauphiné twins. Our misorientation analysis (Figure 11–14) shows that except for relict grains from sample 3B2, low-angle (< 15°) misorientation is not prominent in the Puga Gneiss. This would mean that formation of subgrains through recovery was not dominant (Lloyd, 2004). Similarly, GBM, which operates at higher temperatures, can also be ruled out as regime where majority of Dauphiné twins have developed as the TMCC was undergoing exhumation and, therefore, experienced continuous deformation in progressively lower temperature. Therefore, signature of GBM is more likely to be largely obliterated in the recrystallized set of quartz grains. Although Dauphiné twinning in the relict grains at higher metamorphic grade cannot be ruled out, it can be argued that Dauphiné twins in the recrystallized suites of quartz grains in the Puga Gneiss developed at relatively low temperature of greenschist facies conditions during retrogression of the TMCC. It may also be noted that the differential stress estimated from the recrystallized grains (Table. 1) is similar to the magnitude expected for mechanical Dauphiné twinning (Wenk et al. 2007; Menegon et al. 2011).

One important effect of Dauphiné twinning is localization of dynamic recrystallization in the *r*-twin bands (Menegon et al. 2011). This effect of strain localization due to Dauphiné twinning in GBM or SGR regimes has been documented in the past (Lloyd, 2004; Menegon et al. 2011; Morales et al. 2011; McGinn et al. 2020). These studies have highlighted the importance of Dauphiné twins in strain localization in mid-crustal shear zones. Our study shows ubiquitous presence of Dauphiné twins in both the relict and recrystallized suites of grains. Therefore, we suggest that Dauphiné twins in the relict quartz grains may have developed at any, if not multiple, stages of the complex metamorphic history of the TMCC. As a result, attributing Dauphiné twins in the relict quartz grains of the Puga Gneiss to a particular dynamic recrystallization regime or strain localization is not possible. However, our petrographic observations reveal presence of alternate bands of coarse and fine-grained quartz-rich aggregates that lie parallel to the tectonic foliation defined by muscovite and biotite (Figures 4c, 6a, g, j). These bands are evidence of grain size reduction and strain localization. Abundance of Dauphiné twins in recrystallized quartz grains (Figure 12) indicates that Dauphiné twinning played an important role in grain size reduction and dynamic recovery and recrystallization of quartz aggregate during retrogression/late-stage exhumation of the TMCC. It also emphasizes the role of mechanical twinning in quartz in the overall rheological behaviour of the crust in a collisional zone.

Quartz LPO analysis for relict quartz grains shows that all samples from Karzok zone, two from Central zone (2B2, 2C1) and one sample from the Zildat zone (3A1) have multiple <c> axis maxima that don't provide any meaningful tectonic interpretation (Figure 9). It can be argued that relict quartz grains from these six samples have multiple/mixed slip system activations that have developed during different stages of deformation/metamorphism.

https://doi.org/10.1017/S0016756823000560 Published online by Cambridge University Press

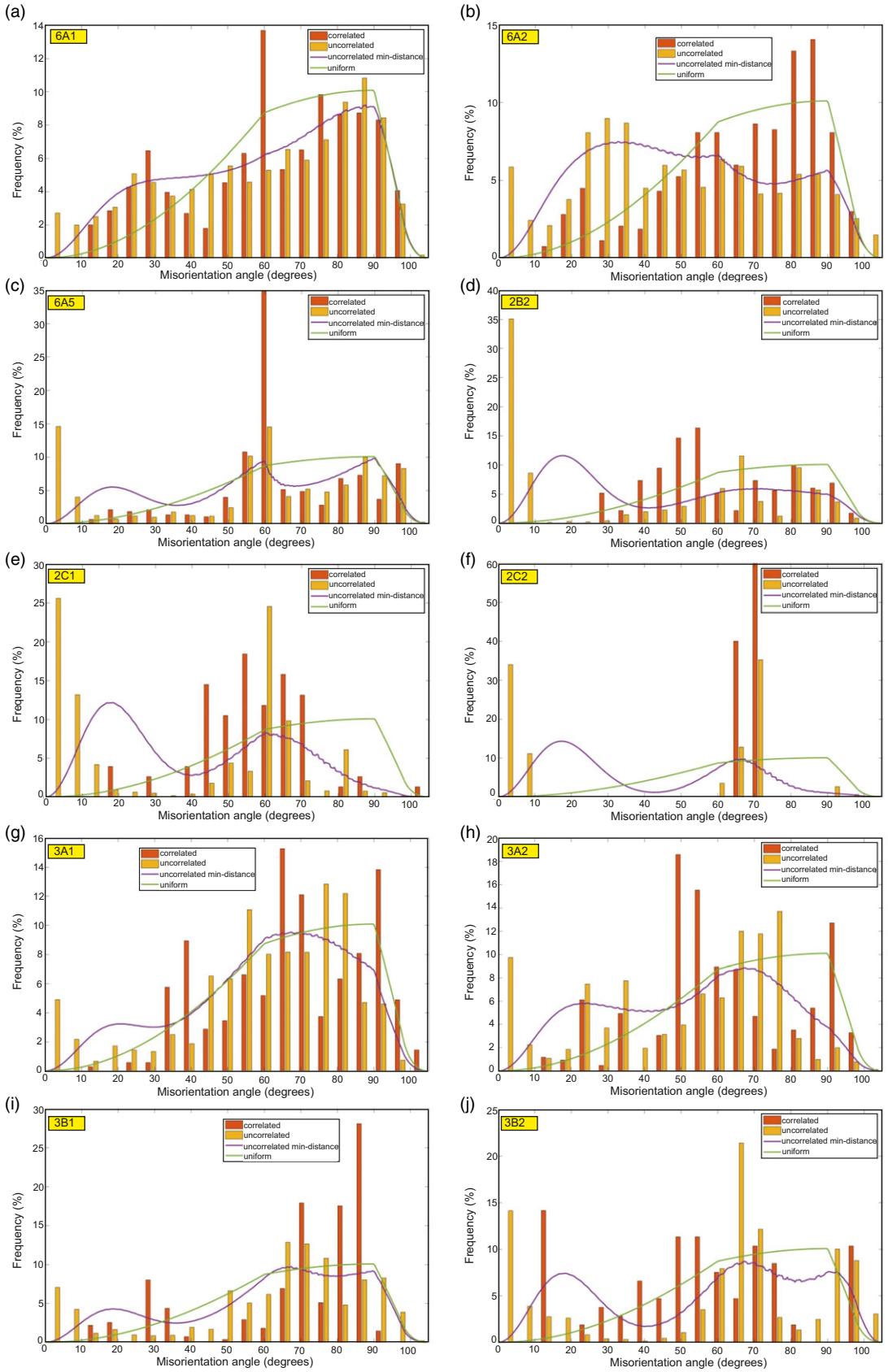

Figure 11. (Colour online) Histogram showing quartz misorientation angle distribution for relict grains.

https://doi.org/10.1017/S0016756823000560 Published online by Cambridge University Press

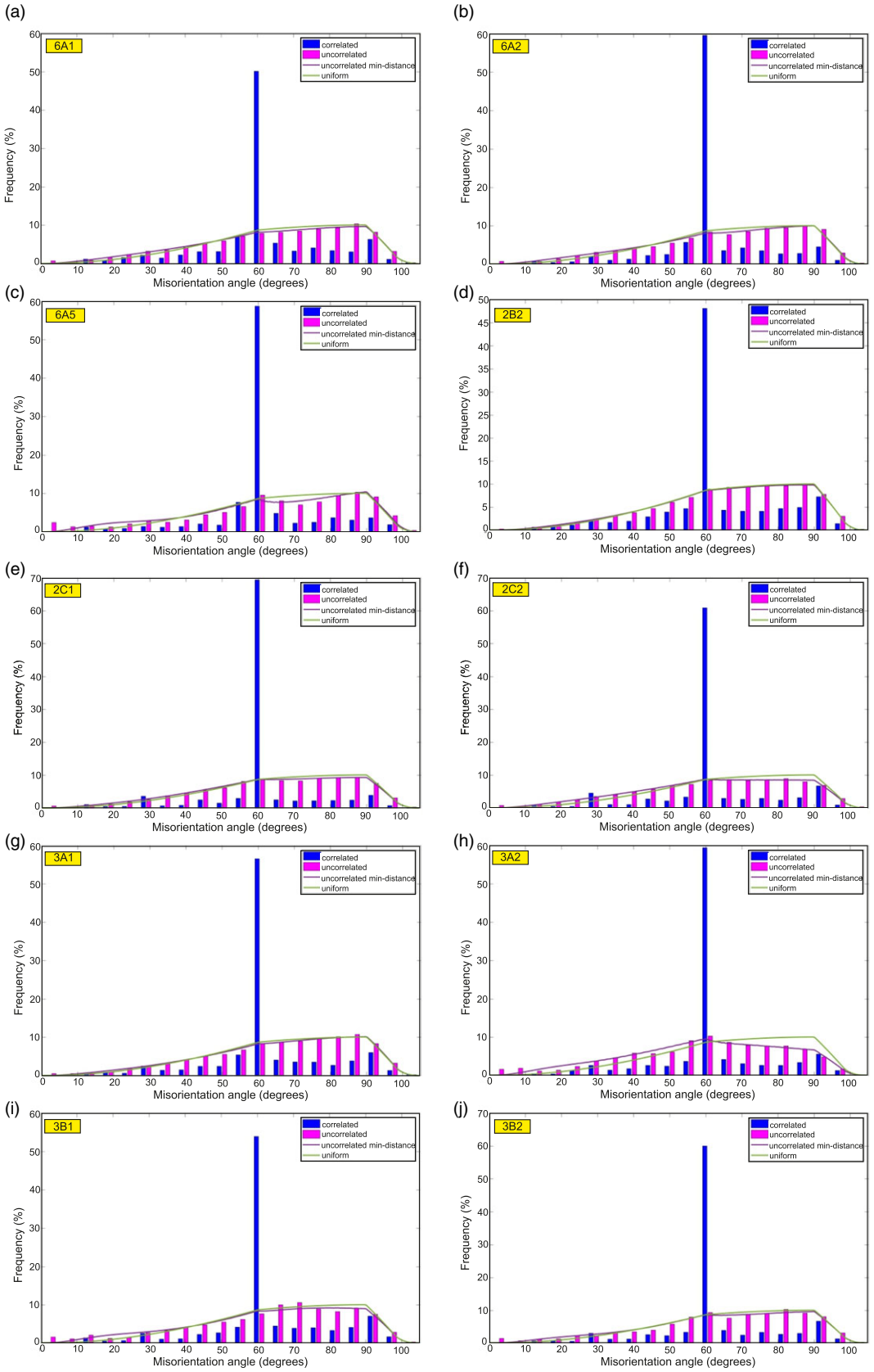

Figure 12. (Colour online) Histogram showing quartz misorientation angle distribution for recrystallized grains.

https://doi.org/10.1017/S0016756823000560 Published online by Cambridge University Press

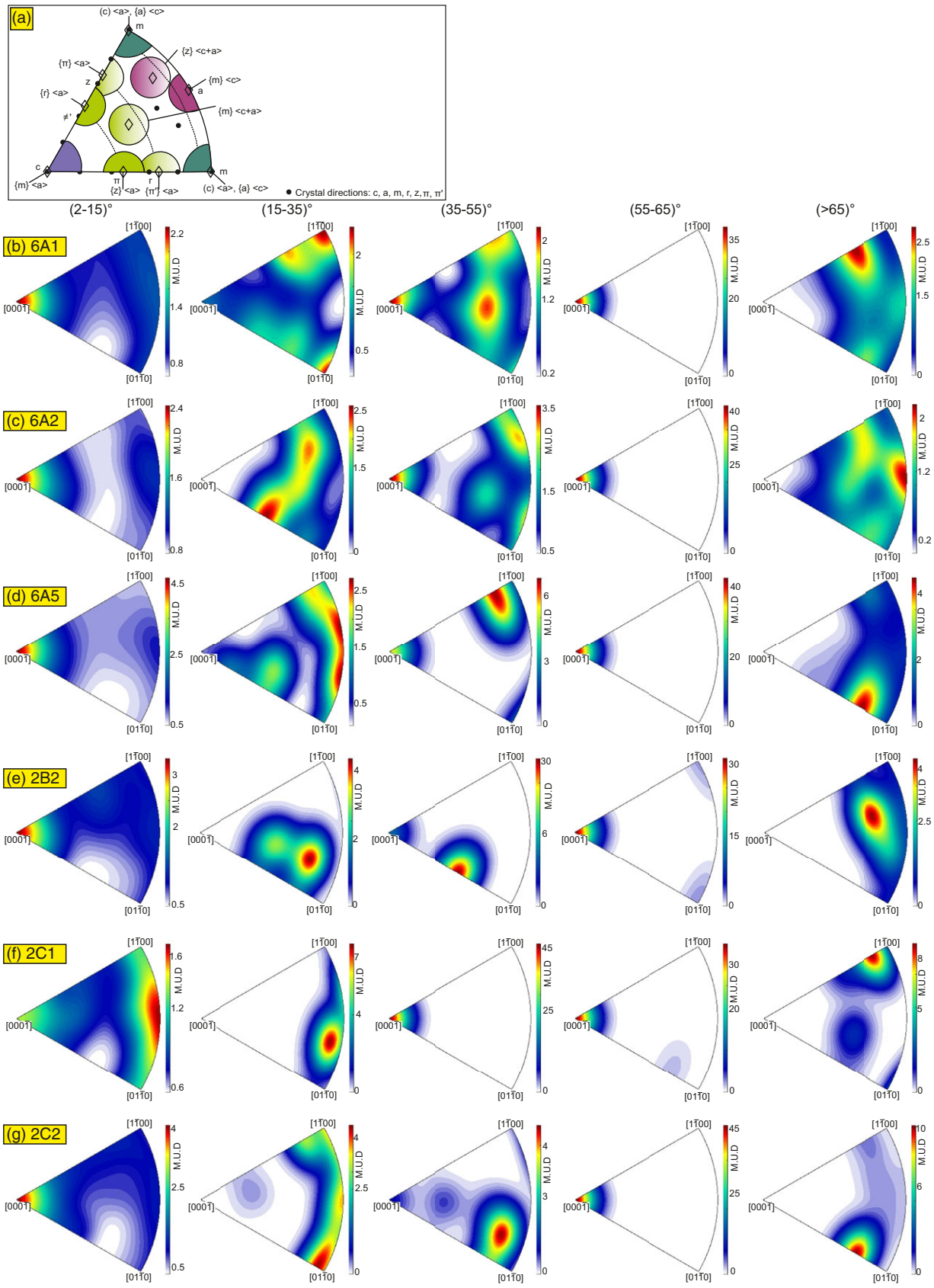

Figure 13. (Colour online) (a) Slip system conventions according to misorientation (after Neumann, 2000). (b–k) Misorientation axis/angle pairs for quartz displayed in crystal coordinates (relict grains, inverse pole figure).

https://doi.org/10.1017/S0016756823000560 Published online by Cambridge University Press

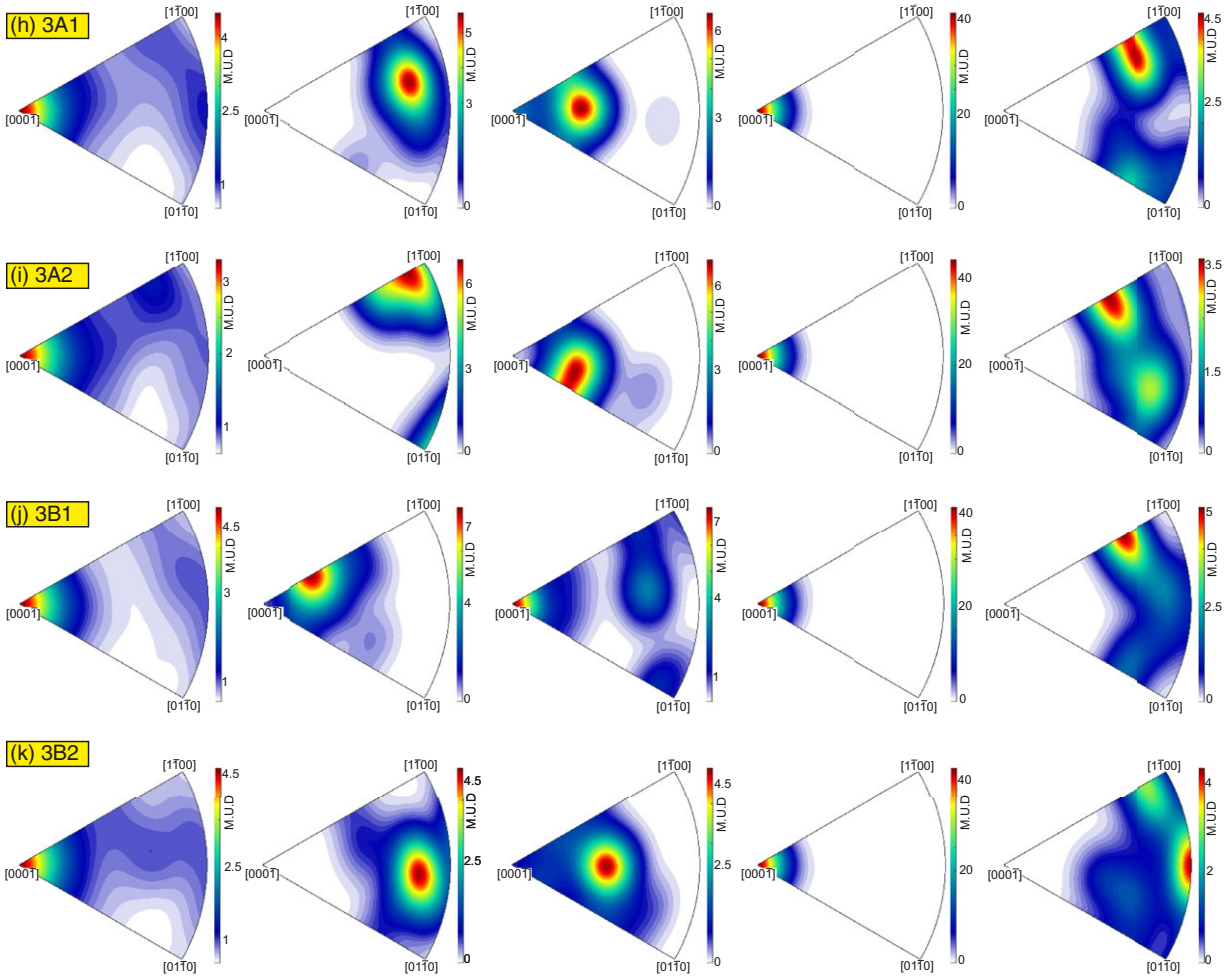

Figure 13. (Continued).

Sample 3B1 has symmetric single girdle and a point maxima around z-axis suggesting activation of both rhomb and prism <a-slip> that may have developed at a temperature of ≤ 500°C (Stipp et al. 2002a). However, three samples from the Zildat zone and sample 2C2 from the Central zone show asymmetric single girdle distribution of the <c> axis (Figure 9), which is indicative of non-coaxial or simple shear (Schmid & Casey, 1986; Thigpen et al. 2010). This distribution is also suggestive of rhomb <a> slip, which once again indicates that this simple shear environment is prevailed at a lower (≤ 500°C) temperature and at a later part of metamorphic evolution of the TMCC. In case of recrystallized grains, this asymmetric single girdle distribution of the <c> axis is more pronounced in the Karzok zone (Figure 10) and samples 3A1 and 3B2 of Zildat zone (Figure 10). This pattern of <c> axis distribution of recrystallized quartz grains, in proximity of the two binding fault zones, helps envisage a simple shear environment in the marginal parts of the TMCC during retrogression and final stage of exhumation.

As mentioned earlier, quartz microstructures and LPO patterns have been studied extensively in the recent past from both the Puga Gneiss (Long et al. 2020; Dutta & Mukherjee, 2021) as well as the eclogitic enclaves embedded within the Puga Gneiss (Dey et al. 2022). Long et al. (2020) carried out finite strain analysis of quartz from the Puga Gneiss. They envisaged a protracted exhumation facilitated by shearing perpendicular to India-Asia convergence that resulted from strain partitioning due to oblique convergence. Dutta & Mukherjee (2021) also suggested transpressional tectonics during India-Asia convergence that helped the TMCC to exhume through a combination of mid-crustal channel flow and wedge extrusion mechanism. Dey et al. (2022) focused on the high-pressure eclogitic enclaves and suggested that subduction/peak metamorphism of the TMCC took place in a constrictional strain regime that changed to plane strain during exhumation. Our study suggests that the Zildat and the Karzok faults played an important role during final stage of exhumation of the TMCC and a simple shear environment persisted during its final clockwise retrograde *P-T* evolution at a temperature ≤ 500°C.

7. Conclusions

Based on the results obtained in the present study, the following conclusions can be drawn:

The relict quartz grains of the Puga gneiss developed deformational microstructures at various stages of metamorphism of the TMCC at a temperature range of 270°C–600°C.

Dauphiné twinning played an important role in progressive grain size reduction and overall deformation of the Puga Gneiss quartz.

Asymmetric single girdle distribution in LPO of recrystallized quartz <c> axis suggests a simple shear environment during final

https://doi.org/10.1017/S0016756823000560 Published online by Cambridge University Press

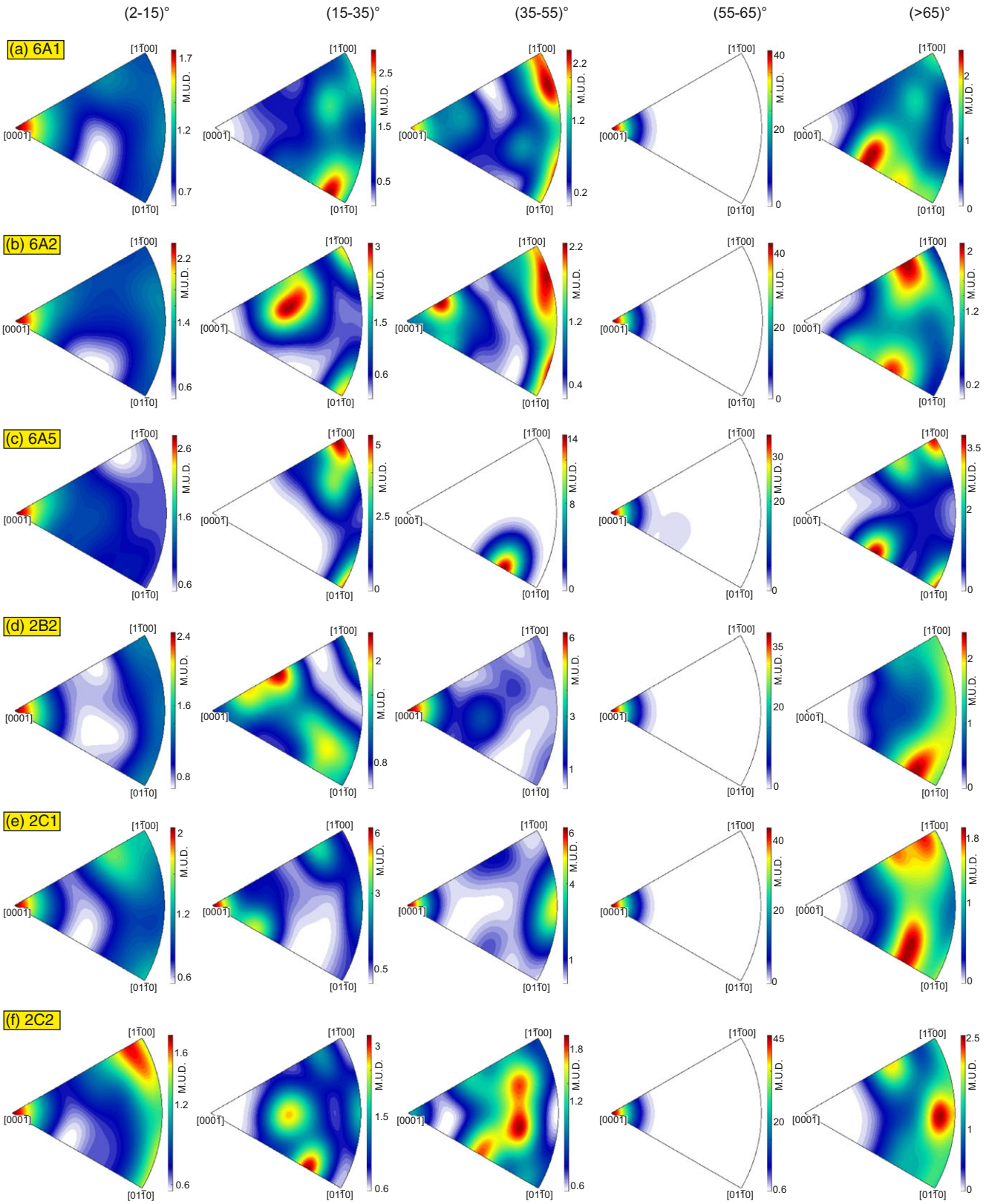

Figure 14. (Colour online) Misorientation axis/angle pairs for quartz displayed in crystal coordinates (recrystallized grains, inverse pole figure).

https://doi.org/10.1017/S0016756823000560 Published online by Cambridge University Press

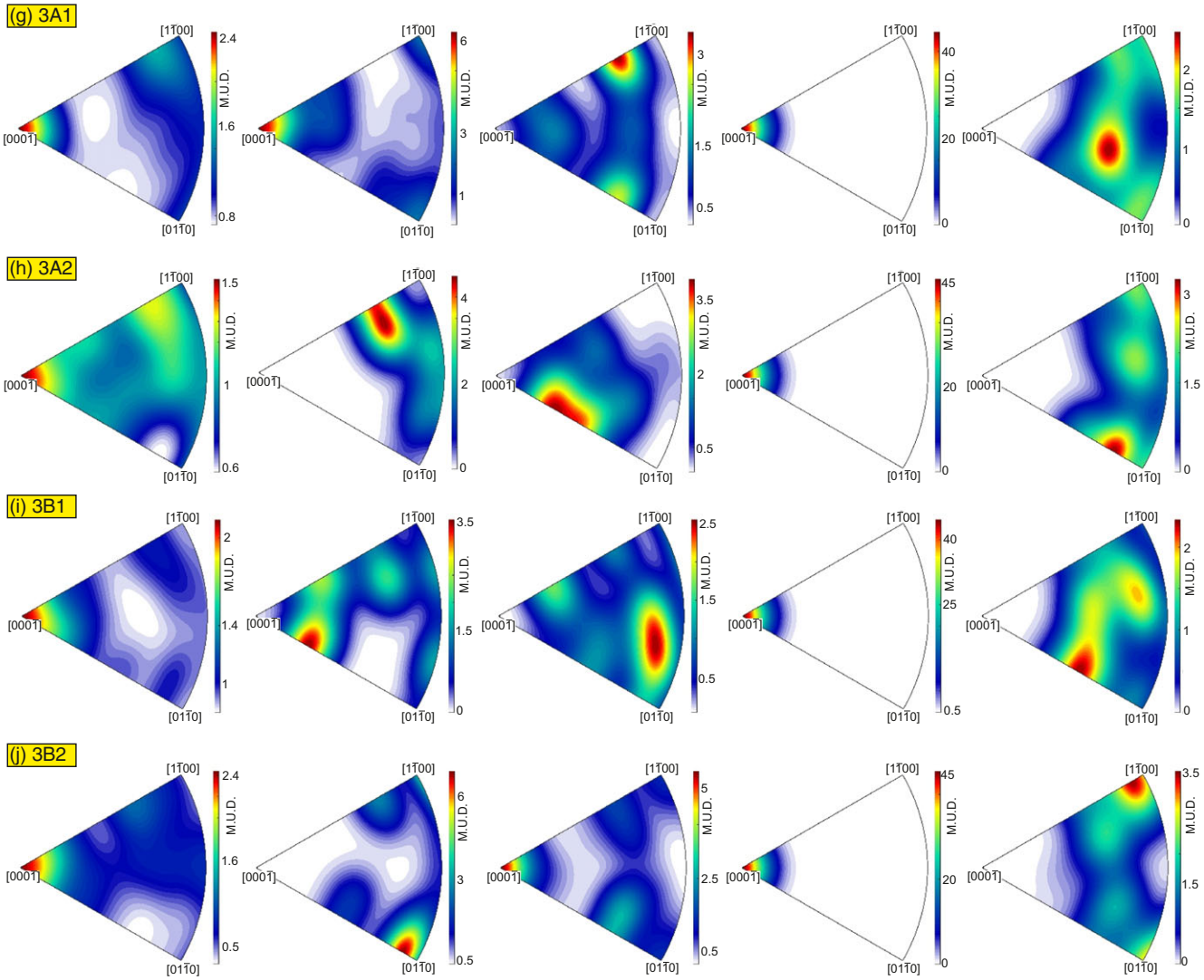

Figure 14. (Continued).

stages of exhumation of the TMCC aided by its two binding fault zones, i.e. the Karzok and the Zildat faults.

Acknowledgement. Director of WIHG is thanked for their encouragement and support. We gratefully acknowledge research grant provided by Ministry of Earth Sciences, Govt. of India (MoES/P.O./Geo/96/2017) for this study. Niloy Bhowmik is thanked for carrying out the EBSD analyses at IIT Kharagpur. Shubham Choudhary is thanked for his help during fieldwork. C. P. Dorje provided logistic support for fieldwork in Ladakh. Tim Johnson is thanked for editorial handling. Critical reviews provided by two anonymous reviewers are gratefully acknowledged. This work is part of the 1st author's ongoing doctoral research work on the TMCC.

Financial support. Ministry of Earth Sciences, Govt. of India (MoES/P.O./Geo/96/2017).

Competing interests. All the authors declare no competing interests.

References

Cross AJ, Kidder S and Prior DJ (2015) Using microstructures and TitaniQ thermobarometry of quartz sheared around garnet porphyroclasts to evaluate microstructural evolution and constrain an Alpine Fault Zone geotherm. *Journal of Structural Geology* **75**, 17–31.

Cross AJ, Prior DJ, Stipp M and Kidder S (2017) The recrystallized grain size piezometer for quartz: an EBSD-based calibration: EBSD-Based Quartz Grain Size Piezometer. *Geophysical Research Letters* **44**, 6667–6674.

de Sigoyer J, Chavagnac V, Blichert-Toft J, Villa IM, Luais B, Guillot S, Cosca M and Mascle G (2000) Dating the Indian continental subduction and collisional thickening in the northwest Himalaya: multichronology of the Tso Morari eclogites. *Geology* **28**, 487–490.

de Sigoyer J, Guillot S, Lardeaux J-M and Mascle G (1997) Glaucophane-bearing eclogites in the Tso Morari dome (eastern Ladakh, NW Himalaya). *European Journal of Mineralogy* **9**, 1073–1084.

Dey A, Sen K and Mamtani MA (2022) Electron backscatter diffraction study of ultrahigh-pressure Tso Morari Eclogites (Trans-Himalayan Collisional Zone): implications for strain regime transition from constrictional to plane strain during exhumation. *Lithosphere* **2022**, 7256746.

Dutta D and Mukherjee S (2021) Extrusion kinematics of UHP terrane in a collisional orogen: EBSD and microstructure-based approach from the Tso Morari Crystallines (Ladakh Himalaya). *Tectonophysics* **800**, 228641.

Epard J-L and Steck A (2008) Structural development of the Tso Morari ultra-high pressure nappe of the Ladakh Himalaya. *Tectonophysics* **451**, 242–264.

Faleiros FM, Campanha GAC, Pavan M, Almeida VV, Rodrigues SWO and Araújo BP (2016) Short-lived polyphase deformation during crustal thickening and exhumation of a collisional orogen (Ribeira Belt, Brazil). *Journal of Structural Geology* **93**, 106–130.

https://doi.org/10.1017/S0016756823000560 Published online by Cambridge University Press

Gilotti JA (2013) The realm of ultrahigh-pressure metamorphism. *Elements* **9**, 255–260.

Giorgis S, Michels Z, Dair L, Braudy N and Tikoff B (2017) Kinematic and vorticity analyses of the western Idaho shear zone, USA. *Lithosphere* **9**, 223–234.

Girard M and Bussy F (1999) Late Pan-African magmatism in the Himalaya : new geochronological and geochemical data from the Ordovician Tso Morari metagranites (Ladakh, NW India). *Schweizerische mineralogische und petrographische Mitteilungen* **79**, 399–418.

Guillot S, De Sigoyer J, Lardeaux JM and Mascle G (1997) Eclogitic metasediments from the Tso Morari area (Ladakh, Himalaya): Evidence for continental subduction during India-Asia convergence. *Contributions to Mineralogy and Petrology* **128**, 197–212.

Guillot S, Hattori KH and de Sigoyer J (2000) Mantle wedge serpentinization and exhumation of eclogites: insights from eastern Ladakh, northwest Himalaya. *Geology* **28**, 199–202.

Hacker BR, Gerya TV and Gilotti JA (2013) Formation and exhumation of ultrahigh-pressure terranes. *Elements* **9**, 289–293.

Hacker BR, Yin A, Christie JM and Davis GA (1992) Stress magnitude, strain rate, and rheology of extended Middle Continental Crust inferred from quartz grain sizes in the Whipple Mountains, California. *Tectonics* **11**, 36–46.

Hazarika D, Paul A, Wadhawan M, Kumar N, Sen K and Pant CC (2017) Seismotectonics of the Trans-Himalaya, Eastern Ladakh, India: constraints from moment tensor solutions of local earthquake data. *Tectonophysics* **698**, 38–46.

Hazarika D, Sen K and Kumar N (2014) Characterizing the intracrustal low velocity zone beneath northwest India–Asia collision zone. *Geophysical Journal International* **199**, 1338–1353.

Heilbronner R and Tullis J (2006) Evolution of c axis pole figures and grain size during dynamic recrystallization: results from experimentally sheared quartzite. *Journal of Geophysical Research* **111**, B10202.

Hielscher R and Schaeben H (2008) A novel pole figure inversion method: specification of the MTEX algorithm. *Journal of Applied Crystallography* **41**, 1024–1037.

Holyoke CW and Tullis J (2006) The interaction between reaction and deformation: an experimental study using a biotite + plagioclase + quartz gneiss: reaction and deformation. *Journal of Metamorphic Geology* **24**, 743–762.

Jaensch SE, Lagoeiro LE, Fossen H and Cavalcante C (2022) Relation between finite strain geometry and quartz petrofabrics in a folded conglomerate in the Norwegian Caledonides. *Journal of Structural Geology* **160**, 104604.

Jessell MW (1987) Grain-boundary migration microstructures in a naturally deformed quartzite. *Journal of Structural Geology* **9**, 1007–1014.

Kilian R and Heilbronner R (2017) Analysis of crystallographic preferred orientations of experimentally deformed Black Hills Quartzite. *Solid Earth* **8**, 1095–1117.

Kohlstedt DL and Weathers MS (1980) Deformation-induced microstructures, paleopiezometers, and differential stresses in deeply eroded fault zones. *Journal of Geophysical Research: Solid Earth* **85**, 6269–6285.

Konrad-Schmolke M, O'Brien PJ, de Capitani C and Carswell DA (2008) Garnet growth at high-and ultra-high pressure conditions and the effect of element fractionation on mineral modes and composition. *Lithos* **103**, 309–332.

Law RD (2014) Deformation thermometry based on quartz <c>axis fabrics and recrystallization microstructures: a review. *Journal of Structural Geology* **66**, 129–161.

Law RD (1990) Crystallographic fabrics: a selective review of their applications to research in structural geology. In Deformation Mechanisms, Rheology and Tectonics (eds RJ Knipe & EH Rutter), pp. 335–352. Geological Society of London, Special Publications no. 54.

Leech M, Singh S, Jain A, Klemperer S and Manickavasagam R (2005) The onset of India–Asia continental collision: early, steep subduction required by the timing of UHP metamorphism in the western Himalaya. *Earth and Planetary Science Letters* **234**, 83–97.

Lister GS and Williams PF (1983) The partitioning of deformation in flowing rock masses. *Tectonophysics* **92**, 1–33.

Lloyd GE (2004) Microstructural evolution in a mylonitic quartz simple shear zone: the significant roles of dauphine twinning and misorientation. In Flow Processes in Faults and Shear Zones (eds GI Alsop, RE Holdsworth, KJW McCaffrey & M Hand), pp. 39–61. Geological Society of London, Special Publications no. 224.

Long SP, Kohn MJ, Kerswell BC, Starnes JK, Larson KP, Blackford NR and Soignard E (2020) Thermometry and microstructural analysis imply protracted extensional exhumation of the Tso Morari UHP Nappe, Northwestern Himalaya: implications for models of UHP exhumation. *Tectonics* **39**, e2020TC006482.

Mainprice D and Nicolas A (1989) Development of shape and lattice preferred orientations: application to the seismic anisotropy of the lower crust. *Journal of Structural Geology* **11**, 175–189.

Mamtani MA, Chakraborty R, Biswas S, Suryawanshi A, Goswami S and Bhatt S (2020) SEM-EBSD analysis of broad ion beam polished rock thin sections – the MFAL protocol. *Journal of the Geological Society of India* **95**, 337–342.

McGinn C, Miranda EA and Hufford LJ (2020) The effects of quartz Dauphiné twinning on strain localization in a mid-crustal shear zone. *Journal of Structural Geology* **134**, 103980.

Menegon L, Piazolo S and Pennacchioni G (2011) The effect of Dauphiné twinning on plastic strain in quartz. *Contributions to Mineralogy and Petrology* **161**, 635–652.

Michels ZD, Kruckenberg SC, Davis JR and Tikoff B (2015) Determining vorticity axes from grain-scale dispersion of crystallographic orientations. *Geology* **43**, 803–806.

Morales LFG, Mainprice D, Lloyd GE and Law RD (2011) Crystal fabric development and slip systems in a quartz mylonite: an approach via transmission electron microscopy and viscoplastic self-consistent modelling. *Geological Society, London, Special Publications* **360**, 151–174.

Neumann B (2000) Texture development of recrystallised quartz polycrystals unravelled by orientation and misorientation characteristics. *Journal of Structural Geology* **22**, 1695–1711.

O'Brien PJ (2019) Tso Morari coesite eclogite: pseudosection predictions v. the preserved record and implications for tectonometamorphic models. In HP–UHP Metamorphism and Tectonic Evolution of Orogenic Belts (eds L Zhang, Z Zhang, H-P Schertl & C Wei), pp. 5–24. Geological Society of London, Special Publications no. 474.

Otani M and Wallis S (2006) Quartz lattice preferred orientation patterns and static recrystallization: natural examples from the Ryoke Belt, Japan. *Geology* **34**, 561–564.

Palin RM, Reuber GS, White RW, Kaus BJP and Weller OM (2017) Subduction metamorphism in the Himalayan ultrahigh-pressure Tso Morari massif: an integrated geodynamic and petrological modelling approach. *Earth and Planetary Science Letters* **467**, 108–119.

Pan R, Macris CA and Menold CA (2020) Thermodynamic modeling of high-grade metabasites: a case study using the Tso Morari UHP eclogite. *Contributions to Mineralogy and Petrology* **175**, 78.

Passchier CW and Trouw RAJ (2005) *Microtectonics*, 2nd ed. Berlin, Heidelberg: Springer. pp. 366.

Paul A, Hazarika D and Wadhawan M (2017) Shear wave splitting and crustal anisotropy in the Eastern Ladakh-Karakoram zone, northwest Himalaya. *Journal of Asian Earth Sciences* **140**, 122–134.

Piazolo S, Prior DJ and Holness MD (2005) The use of combined cathodoluminescence and EBSD analysis: a case study investigating grain boundary migration mechanisms in quartz. *Journal of Microscopy* **217**, 152–161.

Prior DJ, Boyle AP, Brenker F, Cheadle MC, Day A, Lopez G, Peruzzi L, Potts G, Reddy S, Spiess R, Timms NE, Trimby P, Wheeler J and Zetterstrom L (1999) The application of electron backscatter diffraction and orientation contrast imaging in the SEM to textural problems in rocks. *American Mineralogist* **84**, 1741–1759.

Prior DJ, Mariani E and Wheeler J (2009) EBSD in the earth sciences: applications, common practice, and challenges. In *Electron Backscatter Diffraction in Materials Science* (eds AJ Schwartz, M Kumar, BL Adams & DP Field), pp. 345–360. Boston, MA: Springer.

Rahl JM, McGrew AJ, Fox JA, Latham JR and Gabrielson T (2018) Rhomb-dominated crystallographic preferred orientations in incipiently deformed

quartz sandstones: a potential paleostress indicator for quartz-rich rocks. *Geology* **46**, 195–198.

Schmid SM and Casey M (1986) Complete fabric analysis of some commonly observed quartz <c>axis patterns. In Geophysical Monograph Series (eds BE Hobbs and HC Heard), pp. 263–286. Washington, DC: American Geophysical Union.

Skemer P, Katayama I and Karato S (2006) Deformation fabrics of the Cima di Gagnone peridotite massif, Central Alps, Switzerland: evidence of deformation at low temperatures in the presence of water. *Contributions to Mineralogy and Petrology* **152**, 43–51.

St-Onge MR, Rayner N, Palin RM, Searle MP and Waters DJ (2013) Integrated pressure-temperature-time constraints for the Tso Morari dome (Northwest India): implications for the burial and exhumation path of UHP units in the western Himalaya. *Journal of Metamorphic Geology* **31**, 469–504.

Steck A, Epard J, Vannay J, Hunziker J, Girard M, Morard A and Robyr M (1998) Geological transect across the Tso Morari and Spiti areas: the nappe structures of the Tethys Himalaya. *Eclogae Geologicae Helvetiae* **91**, 103–121.

Stipp M and Kunze K (2008) Dynamic recrystallization near the brittle-plastic transition in naturally and experimentally deformed quartz aggregates. *Tectonophysics* **448**, 77–97.

Stipp M, Stünitz H, Heilbronner R and Schmid SM (2002b) The eastern Tonale fault zone: a 'natural laboratory' for crystal plastic deformation of quartz over a temperature range from 250 to 700°C. *Journal of Structural Geology* **24**, 1861–1884.

Stipp M, Stünitz H, Heilbronner R and Schmid SM (2002a) Dynamic recrystallization of quartz: correlation between natural and experimental conditions. In Deformation Mechanisms, Rheology and Tectonics: Current Status and Future Perspectives (eds S de Meer, MR Drury, JHP de Bresser & GM Pennock), pp. 171–190. Geological Society of London, Special Publication no. 200.

Stipp M and Tullis J (2003) The recrystallized grain size piezometer for quartz. *Geophysical Research Letters* **30**, 2088.

Thakur VC and Misra DK (1984) Tectonic framework of the Indus and Shyok suture zones in Eastern Ladakh, Northwest Himalaya. *Tectonophysics* **101**, 207–220.

Thigpen JR, Law RD, Lloyd GE and Brown SJ (2010) Deformation temperatures, vorticity of flow, and strain in the Moine thrust zone and Moine nappe: reassessing the tectonic evolution of the Scandian foreland–hinterland transition zone. *Journal of Structural Geology* **32**, 920–940.

Thomas LA and Wooster WA (1951) Piezocrescence-the growth of Dauphiné Twinning in quartz under stress. Proceedings of the Royal Society of London. Series A, Mathematical and Physical Sciences 208, 43–62.

Trepmann CA, Hsu C, Hentschel F, Döhler K, Schneider C and Wichmann V (2017) Recrystallization of quartz after low-temperature plasticity – the record of stress relaxation below the seismogenic zone. *Journal of Structural Geology* **95**, 77–92.

Trepmann CA and Stöckhert B (2003) Quartz microstructures developed during non-steady state plastic flow at rapidly decaying stress and strain rate. *Journal of Structural Geology* **25**, 2035–2051.

Trepmann CA, Stöckhert B, Dorner D, Moghadam RH, Küster M and Röller K (2007) Simulating coseismic deformation of quartz in the middle crust and fabric evolution during postseismic stress relaxation — an experimental study. *Tectonophysics* **442**, 83–104.

Tullis J (1970) Quartz: preferred orientation in rocks produced by dauphine twinning. *Science* **168**, 1342–1344.

Tullis J and Tullis T (1972) Preferred orientation of quartz produced by mechanical Dauphiné twinning: thermodynamics and axial experiments. In Flow and Fracture of Rocks (eds HC Heard, IY Borg, NL Carter & CB Raleigh), pp. 67–82. Geophysical Monograph Series no. 16.

Tullis J and Yund RA (1985) Dynamic recrystallization of feldspar: a mechanism for ductile shear zone formation. *Geology* **13**, 238–241.

Tullis J and Yund RA (1987) Transition from cataclastic flow to dislocation creep of feldspar: mechanisms and microstructures. *Geology* **4**, 606–609.

Vernooij MGC, den Brok B and Kunze K (2006) Development of crystallographic preferred orientations by nucleation and growth of new grains in experimentally deformed quartz single crystals. *Tectonophysics* **427**, 35–53.

Vollmer FW (1990) An application of eigenvalue methods to structural domain analysis. *Geological Society of America Bulletin* **102**, 786–791.

Warren CJ, Beaumont C and Jamieson RA (2008) Modelling tectonic styles and ultra-high pressure (UHP) rock exhumation during the transition from oceanic subduction to continental collision. *Earth and Planetary Science Letters* **267**, 129–145.

Wenk H-R, Bortolotti M, Barton N, Oliver E and Brown D (2007) Dauphiné twinning and texture memory in polycrystalline quartz: Part 2: In situ neutron diffraction compression experiments. *Physics and Chemistry of Minerals* **34**, 599–607.

Wheeler J, Mariani E, Piazolo S, Prior DJ, Trimby P and Drury MR (2009) The weighted Burgers vector: a new quantity for constraining dislocation densities and types using electron backscatter diffraction on 2D sections through crystalline materials. *Journal of Microscopy* **233**, 482–494.

Wightman RH, Prior DJ and Little TA (2006) Quartz veins deformed by diffusion creep-accommodated grain boundary sliding during a transient, high strain-rate event in the Southern Alps, New Zealand. *Journal of Structural Geology* **28**, 902–918.

Wilke FD, O'Brien PJ, Schmidt A and Ziemann MA (2015) Subduction, peak and multi-stage exhumation metamorphism: Traces from one coesite-bearing eclogite, Tso Morari, western Himalaya. *Lithos* **231**, 77–91.

Wright SI, Nowell MM and Field DP (2011) A review of strain analysis using electron backscatter diffraction. *Microscopy and Microanalysis* **17**, 316–329.

https://doi.org/10.1017/S0016756823000560 Published online by Cambridge University Press